

1 **Forearc crustal faults as tsunami sources in the upper**
2 **plate of the Lesser Antilles subduction zone. The Case**
3 **study of the Morne Piton fault system.**

4 Melody Philippon^{1,*}, Jean Roger², Jean-Frederic. Lebrun¹, Isabelle Thinon³, Océane Foix⁴,
5 Stéphane Mazzotti⁴, Marc-Andre Gutscher⁵, Leny Montheil⁴, Jean-Jacques Cornée⁴.

6 *1. Géosciences Montpellier, Université de Montpellier, CNRS, Université des Antilles, Pointe-*
7 *à-Pitre, French West Indies.*

8 *2. Earth and Structure Processes Department, GNS Sciences, Lower Hutt, New Zealand.*

9 *3. BRGM – French Geological survey, 3 avenue Claude Guillemin 45060 Orléans*

10 *4. Géosciences Montpellier, Université de Montpellier, CNRS, Université des Antilles,*
11 *Montpellier, France.*

12 *5. Geo-Ocean, Univ.Brest, CNRS, Ifremer, Brest, France.*

13 ** Corresponding author : melody.philippon@univ-antilles.fr*

14

15 ***Abstract***

16 In this study, alternatively to the megathrust, we identify upper plate normal faults
17 orthogonal to the trench as a possible tsunami source along the Lesser Antilles
18 subduction zone. The Morne Piton fault system, is such a trench-perpendicular upper
19 crustal fault at the latitude of Guadeloupe. By the means of seismic reflection, high
20 resolution bathymetry, remotely operated vehicle (ROV) imaging and dating, we reassess
21 the slip rate of the Morne Piton fault since 7Ma, *i.e.* its inception, and quantify an average
22 rate of $0.25 \text{ mm}\cdot\text{yr}^{-1}$ since ca. 1.2Ma dividing by two previous estimations and thus
23 increasing the earthquake time recurrence and lowering the associated hazard. ROV dive
24 revealed a metric scarp with striae at the toe of the Morne Piton fault system suggesting
25 a recent fault rupture. We estimate a fault rupture area of $\sim 450\text{-}675 \text{ km}^2$ and then a
26 magnitude range for a maximum seismic event around $M_w 6.5 \pm 0.5$ making this fault
27 potentially tsunamigenic as the nearby Les Saintes Fault responsible for a tsunami
28 following the 2004, $M_w 6.3$ earthquake. Consequently, we simulate a multi-segment
29 tsunami model representative for a worst-case scenario as if the whole identified Morne
30 Piton fault segments ruptured together. Our model provides clues for the potential impact
31 of local tsunamis on the surrounding coastal area as well as for local bathymetric controls

32 on tsunami propagation. We illustrate that (i) shallow water plateaus act as secondary
33 sources and are responsible for a wrapping of the tsunami waves around the island of
34 Marie-Galante, (ii) canyons indenting the shallow water plateau slope break are focusing
35 and enhancing the wave height in front of the most touristic and populated town of the
36 island, (iii) resonance phenomenon is observed within Les Saintes archipelago showing
37 that the waves' frequency content is able to perturbate the sea-level during many hours
38 after the seismic rupture.

39

40 Keywords: subduction zone, forearc, crustal fault, slip rate, tsunami hazard, Lesser
41 Antilles, Guadeloupe Island

42

43 **1. Introduction**

44

45 Regions at the vicinity of active subduction zones are prone to seismic and related
46 hazards, including tsunamis, exposing their inhabitants to multiple threats. Megathrust
47 earthquakes represent the greatest threat with the highest seismic moments and
48 consequently huge tsunamigenic potential (Satake and Tanioka, 1999). Earthquakes
49 triggered on crustal faults in the overriding plate represent an additional hazard that
50 needs to be quantified (Bilek, 2010). In order to assess the hazards and mitigate the risks
51 associated with these crustal faults, it is essential to estimate their slip rates.

52 On land, slip rates on active faults are determined from paleo-seismic trenches (McCalpin,
53 1996), high resolution geophysical investigation (Wallace, 1981; Zhang et al., 2014),
54 satellite imagery (Tronin, 2009), InSAR (Biggs and Wright, 2020), geodetic measurement
55 (GNSS: Symithe et al., 2013) as well as seismicity which account for the present-day strain
56 accumulation of the crust. Offshore, slip rate estimates are provided by the means of
57 underwater geodesy (*i.e.* acoustic geodesy: Kido et al., 2006; Petersen et al., 2019; Fujita
58 et al., 2006) or fiber optic monitoring (Hirata et al., 2002; Gutscher et al., 2019). The
59 recurrence time of events may be estimated by the study of turbidite deposits cores (e.g.,
60 Cascades: Goldfinger et al., 2012; Taiwan: Lehu et al., 2016; Antilles: Seibert et al., 2016;
61 New Zealand: Lewis et al., 1980), high resolution marine seismic and multibeam echo-
62 sounder data (e.g., Escartin et al., 2016, 2018), and submarine dives survey (e.g., Geli et
63 al., 2011). However, constraining hazard models in areas undergoing slow strain rates
64 remains challenging as the earthquakes recurrence time overcomes the historical period.

65 Indeed, geodetic measurements require decades-long time series as the resolution of the
66 method is not accurate enough and erosion or high sedimentation rates may have erased
67 or covered, respectively, the active fault scarps making it difficult to identify active faults
68 segments. Therefore, datasets based on the last ten to hundred years of record along
69 tectonic systems undergoing slow strain rates may not be representative of the bulk
70 strain and may be at the origin of biased estimations of slip rate along these faults.

71 The Lesser Antilles (Eastern Caribbean) records slow deformation rates as the north and
72 south American tectonic plates slowly subduct under the Caribbean plate ($20\text{mm}\cdot\text{yr}^{-1}$ -
73 Figure 1). Extensional tectonics and normal faulting affect the forearc (Feuillet et al.,
74 2002, De Min et al., 2015, Boucard et al., 2021) but available historical data do not report
75 tsunami events related to forearc fault rupture. However, the Les Saintes M_w 6.3
76 earthquake of December 2004 ruptured the Roseau normal fault (Feuillet et al., 2011a,
77 Bazin et al., 2010). The earthquake reached an intensity up to VIII in the Guadeloupe
78 Archipelago (Figure 1), being felt by most of its $\sim 400,000$ inhabitants, and was
79 responsible for one casualty. This earthquake triggered a tsunami with up to 2 m high
80 waves at the coast and a maximum measured run-up distance of 42 m in Les Saintes
81 (Zahibo et al. 2005; Le Friant et al. 2008; Cordrie et al. 2020). Prior to this event, this fault
82 was unmapped and therefore not identified as an active fault (Feuillet et al., 2002; Terrier
83 and Combes, 2002). Forearc normal faults, similar to Les Saintes fault system, may pose
84 a threat to the 4 million inhabitants of the Lesser Antilles that are living on volcanic arc
85 islands facing the subduction trench to the east and literally sitting over the subduction
86 interface.

87 The present study focuses on the Morne Piton fault system, perpendicular to the
88 subduction trench, which is one of the most prominent onshore-offshore fault systems
89 which cuts the Guadeloupe Archipelago arc and forearc islands (Figure 1). Regarding the
90 seismic and tsunami hazards related to this fault system and the vulnerability of the
91 coastal population and infrastructures of the archipelago, the objectives are to (1)
92 estimate the fault slip rate (2) determine the geometry of the fault segments, and (3)
93 model the associated tsunami hazard, since such a joint approach has been lacking so far.
94 In the following study, the fault geometry is refined in order to provide an up-to-date map
95 of the fault segments thanks to high-resolution (HR) bathymetric data. Then, we integrate
96 its long-term slip rate over the last *ca.* 7 My, *i.e.* from fault initiation to present-day, by the
97 mean of HR seismic reflection lines and available biostratigraphic and isotopic dates.

98 Secondly, Remotely Operated Vehicles (ROV) explorations of seafloor rupture allowed us
99 to measure the height of the fault scarp and to determine the fault kinematics from
100 striations observed along a recent co-seismic scarp. Because the overall geometry of this
101 fault system is comparable to the Les Saintes fault system in terms of length, seafloor
102 scarp and dip, we postulate that a rupture along the Morne Piton fault may trigger a local
103 tsunami close to the coasts of the Guadeloupe Archipelago. Therefore we study the
104 seismogenic and tsunamigenic potential of the Morne Piton fault system providing an
105 overview of what could happen in terms of tsunami generation if all the segments of the
106 Morne Piton fault ruptured simultaneously, *i.e.* a plausible worst-case scenario. This
107 scenario allows to identify and discuss the local bathymetric controls on the propagation
108 of the resulting tsunami wave and the consequences (*e.g.*, amplifications and
109 interferences) in near-shore areas of the neighboring populated islands. We do not assess
110 coastal inundation scenarios, as our scenario can't be refined by observational rupture
111 data accurate enough to realize such a specific hazard study. Finally, we conclude on the
112 importance of forearc crustal faults as potential major tsunami sources in subduction
113 zones.

114

115 **2. Geological settings**

116

117 Oceanic lithosphere of the North and South American plates is slowly subducting
118 beneath the Caribbean plate at a convergence rate of $\sim 20\text{mm}\cdot\text{yr}^{-1}$ (Figure 1, DeMets et al.,
119 2000; Philippon and Corti, 2016). The convex trench geometry results in along strike
120 variations of obliquity, increasing northward from Guadeloupe. Along the arc, oblique
121 subduction is accommodated by trench-parallel left-lateral strike slip faults such as the
122 Harvers-Montserrat-Bouillante / Les Saintes corridor (located within the volcanic arc),
123 the Bunce fault (located along the crustal buttress), and a series of trench-perpendicular
124 grabens forming a sinistral horsetail (Feuillet et al., 2002; Feuillet et al., 2010; Ten Brink
125 et al., 2004; Laurencin et al., 2019; Boucard et al., 2021) (Figure 1, Figure 2A).

126 In the central Lesser Antilles, the Marie-Galante Basin (Guadeloupe Archipelago),
127 is located at the southern end of the aforementioned regional horsetail system and is
128 described as a conjugated normal fault system defining a trench perpendicular graben
129 (Figure 2 A; Feuillet et al., 2001, 2011). This graben affects sediment deposits comprising
130 three regional mega-sequences: an Eocene(?) - Early Miocene MG-MS1 sequence, a mid-

131 Miocene – late Tortonian / early Messinian MG-MS2 sequence, and a Messinian to present
132 MG-MS3 sequence (Bouysse et Mascle, 1994; De Min, 2014; De Min et al., 2015; Cornée et
133 al., 2023). It shapes the Marie-Galante Basin (up to 1200 m water depth) and
134 surroundings, Grande-Terre and Marie-Galante Islands, respectively (Figure 1). The
135 northern boundary of the Marie-Galante Basin is the east trending, south dipping Gosier
136 fault that runs primarily onshore along the southern coast of Grande-Terre (Garrabé and
137 Andreieff, 1988; Figure 2A). The southern boundary of the basin consists of the N100°
138 trending, ~50 km-long, north dipping Morne Piton fault, which crosscuts the northern
139 edge of Marie-Galante Island (Bouysse et al., 1993) and extends offshore on both sides of
140 the island (Feuillet et al., 2002, 2004).

141 The Morne Piton fault system consists of five main 5-15 km-long segments
142 trending N90°E ± 30° separated by N140°E shorter right-lateral relays (Figure 2). The
143 fault scarp is exposed at Anse Piton, eastern coast of Marie-Galante, and shows dip-slip
144 striations (Feuillet et al., 2002). Onshore Marie-Galante, the fault offsets the Pliocene to
145 middle Pleistocene platform by ~60 m. It also crosscuts a series of 3 uplifted late-mid to
146 late Pleistocene terraces along the eastern side of the island. Feuillet et al. (2004)
147 calculated a 5 km dislocation depth and a 70 to 80°N fault dip to model the observed
148 flexure of the footwall. Considering that the Marie-Galante Plateau is a flat abandoned
149 330 Ka old marine terrace, these authors estimate the average slip rate of the Morne Piton
150 at about 0.5±0.2 mm·yr⁻¹ since 330 Ka. Regarding the uplifted terraces they estimated a
151 maximum earthquake moment magnitude (M_w) ranging from 5.8 up to 6.5 with a 400-
152 1000 to 1400-3300 years of recurrence time, respectively (250 km² of estimated
153 ruptured area). Moreover, it was later demonstrated that this plateau emerged between
154 1.77 and 1.07 Ma (magnetostratigraphic Chron 1R2r: Cornée et al., 2012; Münch et al.,
155 2014; De Min et al., 2015; Léticée et al., 2019; Cornée et al., 2021). Note that considering
156 an older age for the Plateau emergence would drastically lower the slip rate estimate and
157 increase the recurrence time calculated by Feuillet et al. (2001).

158

159 ***3. Historical seismicity***

160

161 Upper plate seismicity in the Marie-Galante Basin provided by (i) CDSA Seismic
162 database (Antilles Seismological Data Center - Bengoubou-Valerius et al. (2008); Massin et
163 al.(2021)), (ii) IRIS database (IRIS <https://www.isc.ac.uk> (Figure 2B) and (iii) the

164 deployment of Ocean Bottom Seismometers (OBS) (Ruiz et al., 2013; Bie et al., 2019)
165 shows a widely distributed pattern of moderate magnitude earthquakes ($M_w \leq 5.3$), with
166 the exception of the 2004 seismic cluster in Les Saintes. Wide Angle Seismic (WAS)
167 profiles together with earthquakes data indicate a seismogenic crustal thickness limited
168 to the first 15-20 km west of Marie-Galante suggesting a brittle-ductile transition at this
169 depth (Kopp et al., 2011; Ruiz et al., 2013; Gonzalez et al., 2017; Padron et al., 2021).
170 Among the very few focal mechanisms available in the Marie-Galante Basin (Gonzalez et
171 al., 2017), the 25 February 2014 M_w 3.8 earthquake occurred beneath the southern
172 Grande-Terre platform and shows pure normal motion along sub-E-W trending nodal
173 planes (Gonzalez et al. 2017, Event n°9, hypocentral location accuracy of ca. 5 km; Figure
174 2C). The location, depth and nodal plane characteristics (57° dip and $N102^\circ E$) of the
175 earthquake indicate that the event may correspond to a rupture along the Gosier fault
176 system, which is the only major fault system in the vicinity of the hypocentral location
177 able to trigger such magnitude earthquake. Feuillet (2000) provided more than 20 focal
178 mechanisms for earthquakes showing local magnitude $2 < M_l < 3.7$ and one $M_s = 5.6$
179 earthquake, located in and around the Marie-Galante Graben. All focal mechanisms show
180 nearly pure normal motion along sub-E-W trending nodal planes, consistent with
181 kinematics indicators observed along the Gosier and Morne Piton faults. This tectonic
182 pattern is confirmed by GNSS velocities which indicate that a small trench-parallel
183 extension is accommodated in the upper plate forearc (van Rijsingen et al., 2021).

184 Two historical earthquakes are reported along these two fault systems: (i) the 16
185 May 1851 earthquake with a maximum intensity of VII recorded in the southeastern part
186 of Basse-Terre, is attributed to the Morne Piton fault with an estimated moment
187 magnitude $M_w = 6.0$ (Feuillet et al., 2011; and (ii) the 29 April 1897 earthquake with a
188 maximum intensity of VIII recorded in the Pointe-à-Pitre area being either attributed to
189 the Gosier Fault system with an estimated moment magnitude $M_w = 5.5$, or to the
190 Montserrat fault zone, with an estimated moment magnitude $M_w = 6.5$ (Bernard and
191 Lambert, 1988; Feuillet et al., 2011b). Overall, at the latitude of Guadeloupe, regional
192 earthquake data suggests that normal fault systems are active with an ability to generate
193 earthquakes of moment magnitude M_w 6 and above. This magnitude range is potentially
194 able to trigger tsunami according to tsunami catalogues (as explained, for example, in
195 Roger et al., 2019).

196

197

198 **4. Historical tsunami**

199

200 Southwest of the Marie-Galante Basin, the 2004 M_w 6.3 earthquake (Bazin et al.,
201 2010; Feuillet et al., 2011) showed that upper plate crustal faults can generate strong
202 earthquakes and tsunamis. The main shock occurred along the NNW-SSE trending, *ca.* 40
203 km-long arc-parallel Les Saintes Fault System (Feuillet et al., 2011; Leclerc et al., 2016).
204 The recurrence of such a rupture is estimated to be a few hundred years or more (Escartin
205 et al., 2016; Escartin et al., 2018; Feuillet et al., 2011; Le Friant et al., 2008). Focal
206 mechanisms of the main shock as well as five aftershocks provided an overall pure
207 normal motion along NNW-SSE nodal planes (Figure 2D). Source models from Salichon
208 et al. (2009), Bazin et al. (2010), and Feuillet et al. (2011), well constrained by the long
209 duration of the aftershock sequence, proposed a main source localized along the N135°E
210 trending, 50°E dipping Roseau Fault (westernmost fault of Les Saintes fault system) with
211 a 30 km-long and 21 km-downdip width fault plane. Aftershock seismicity reactivated
212 several nearby conjugate faults with a maximum seismic depth at *ca.* 15 km. The main
213 rupture occurred at two asperities located 8 km below the surface with a maximum slip
214 of 1.8 m, and propagated to the surface triggering a coseismic offset of the seafloor of 0.3-
215 0.6 m along a *ca.* 10 km-long segment. Escartin et al. (2016) investigated the fault scarp
216 by the mean of HR bathymetry highlighting a 3 km-long, up to 0.9 m-high scarp, but
217 concluded that part of the observed slip may be post-seismic. The Les Saintes earthquake
218 generated up to 2 m-high tsunami waves at the coast and a maximum horizontal run-up
219 of 42 m in some bays of Les Saintes (Zahibo et al., 2005; Le Friant et al., 2008; Cordrie et
220 al., 2020). However, tsunami models using fault parameters based on seismological data
221 resulted in an underestimation of the tsunami wave amplitude and run-up (Le Friant et
222 al., 2008). Cordrie et al. (2020) consider that their best fit models require greater slip on
223 the fault plane and a greater magnitude for the earthquake than those given by the
224 seismological data in order to accurately reproduce the observed tsunami, suggesting
225 that the observed scarp is the surface expression of co-seismic slip (source parameters:
226 M_w =6.4-6.5 – fault plane 15x15 km – Strike N325°E – Dip 55°E – rake *ca.*90° - slip=2.5-
227 3.5 m).

228 Over the last ~500 years of historical written archives in the Lesser Antilles, a few
229 dozen confirmed tsunamis from different origins (local, regional or far-field sources

230 including earthquakes, landslides, volcanic eruptions or combinations of them) have
231 been reported. Starting with the 16 April 1690 $M_s \sim 8.0$ Barbados earthquake (which
232 presumably triggered the first reported tsunami in the Lesser Antilles), it includes the
233 widely studied 1 November 1755 Lisbon transoceanic tsunami (*e.g.*, Gutscher et al., 2006,
234 Accary and Roger, 2010; Roger et al., 2010, 2011, Martinez-Loriente et al., 2021) and the
235 18 November 1867 Virgin Islands tsunami (*e.g.*, Zahibo et al., 2003, 2005; Barkan and ten
236 Brink, 2004). Landslide sources and/or pyroclastic flows, are also known for their
237 tsunamigenic potential. There are more and more studies led to assess the hazard
238 associated to these “silent tsunamis” (*e.g.*, Roger et al., 2024). In the Caribbean Region, a
239 few tsunamis triggered by landslides and/or pyroclastic flows have been reported in
240 catalogues of events (*e.g.*, O’loughlin and Lander, 2003; Accary and Roger, 2010),
241 bathymetric surveys helped to identified large submarine landslide scars and deposits
242 (*e.g.*, Deplus et al., 2001; Le Friant et al., 2009, 2019) and a few studies have highlighted
243 the capacity of these landslides to trigger large tsunamis (*e.g.*, Smith and Shepherd, 1996;
244 Teeuw et al., 2009; Leslie and Mann, 2016).

245 On the basis of an extensive literature review, including cross-checking of
246 information, we conclude that only four tsunamis reported in Guadeloupe are likely of
247 upper crustal seismic origin (Mallet, 1853, 1854, 1855; Lander, 1997; Zahibo and
248 Pelinovsky, 2001; Lander et al., 2003; O’Loughlin and Lander, 2003; Zahibo et al., 2003;
249 Accary and Roger, 2010; Nikolkina et al., 2010; Roger et al., 2013; online databases:
250 NGDC/WDS, 2023; TL/ICMMG, 2023). These tsunamis have been observed or recorded
251 following earthquakes occurring on regional faults (indicated magnitude and epicenter
252 coordinates are from the USGS online earthquakes catalogue:
253 <https://www.usgs.gov/programs/earthquake-hazards>): the $M_w \sim 8.0-8.5$ earthquake on
254 8 February 1843 (NE of Guadeloupe, 16.73°N, 61.17°W) and the M_w 7.2 earthquake on 25
255 December 1969 (SE of Guadeloupe, 15.648°N, 59.694°W) are arguably attributed either
256 to a rupture along the megathrust or to upper plate faulting ; the M_w 6.5 earthquake on
257 16 March 1985 (along the Harvers-Montserrat-Bouillante fault system between
258 Montserrat and Nevis, north of Basse-Terre, 17.013°N, 62.448°W); and the M_w 6.3
259 earthquake on 21 November 2004 (Along the Les Saintes fault system, south of Basse-
260 Terre, 15.679°N, 61.706°W)(Figure1). The largest earthquakes and tsunamis produced
261 at subduction zones are expected to originate from rupture at the plate interface
262 megathrust. However, historical records in the Lesser Antilles reveal that neither the

263 1843 M_w 7.5-8.5 nor the 1839 M_w 7.5-8.5 largest known earthquakes, although
264 destructive, have been followed by large tsunamis. However, Roger et al. (2013) showed
265 that the simulation of a M_w 8.5 1843-like megathrust earthquake would have produced
266 wave amplitudes of 5 m and more along the exposed coasts of Guadeloupe, which was not
267 reported in coeval documents. Feuillet et al. (2011) explain these two major earthquakes
268 by the great depth of the rupture along the megathrust that led to little seafloor
269 deformation. However, numerical simulation of worst-case scenarios for these two
270 ruptures along the megathrust evidence the possibilities of tsunami amplitudes up to 10
271 meters and above in some embayment (Roger et al., 2013; Colon-Useche et al., 2023. As
272 magnitude of crustal earthquakes is constrained by fault length, events occurring along
273 such crustal fault show a much smaller magnitude than megathrust earthquakes
274 consequently may form smaller seafloor offsets. Thus, most crustal earthquakes able to
275 trigger a tsunami do not produce significant sea surface deformation (only a few
276 centimeters amplitude in most cases) compared to subduction interface earthquakes.
277 Associated tsunamis are typically only visible on pressure gauge records (coastal gauges
278 or DART systems) after processing the data (*e.g.*, de-tiding, high-frequencies filtering,
279 etc.).

280

281 **3. Material and method**

282

283 **3.1 Seismic lines**

284 We present eight multichannel seismic (MCS) lines acquired during five
285 oceanographic campaigns (location on Figure 3A). These include high-resolution sparker
286 source seismic data from KaShallow 1 (Lebrun et al., 2009) and GEOBERYX03
287 oceanographic campaigns (Thinon and Bitri, 2003; Thinon et al., 2004 and 2010), mid
288 resolution GI airgun arrays seismic data from KaShallow 2 (Lebrun et al., 2009) and
289 Aguadomar (Deplus et al., 1999) cruises, and deep penetrating MCS data from the
290 Sismantilles 1 seismic experiment (Hirn, 2001) (Table 1).

291 Sismantilles 1 seismic data have been processed using CGG-Veritas Geovector®
292 software on board the R/V Nadir (Hirn et al., 2001). Processing includes band pass
293 filtering, internal and external mute, one step velocity analysis, NMO correction, stack,
294 predictive deconvolution and post-stack constant water-velocity time migration. The

295 KaShallow 1 and 2, Aguadomar and Geoberyx have been processed with Seismic Unix
296 software ([Cohen and Stokwell, Center for Wave Phenomena, Colorado School of Mines](#)).
297 The seismic processing includes band pass filtering, sea waves and spherical divergence
298 corrections, constant velocity or simple velocity gradient NMO correction and stack, and
299 constant water-velocity time migration. The reflection seismic lines are in millisecond
300 two-way-travel-time (mstwt). The velocities of the Wide Angle Seismic refraction (WAS)
301 profiles are in second two-way-travel-time (stwt).

302

303 *3.2 Bathymetry*

304 High-resolution bathymetric data were acquired during the KaShallow2
305 oceanographic campaign (Lebrun, 2009) using a Simrad EM300 multibeam echosounder.
306 We merged this data with Aguadomar (Deplus, 1999) and Sismantilles 2 (Laigle et al.,
307 2007) cruises Simrad EM12 Dual multibeam echosounder data available for the Marie-
308 Galante Basin. Vertical accuracy for these echosounders is plurimetric for typical water
309 depth found in the Marie-Galante Basin (<2000 m below mean sea-level, noted bsl
310 hereafter). Near-shore (0-200 m bsl) and onshore, very high-resolution bathymetric and
311 topographic data comes from the Litto3D database -
312 (<https://www.geoportail.gouv.fr/donnees/litto3d> last accessed on September 2024-
313 that includes airborne lidar survey and KaShallow-3 multibeam data acquired with a
314 RESON Seabat 8101 multibeam echosounder). The vertical accuracy for this second
315 dataset is better than one meter. We used the [Caribes software](#) (ifremer) to process the
316 data and to produce a 25 m grid spacing Digital Elevation Model of the Marie-Galante
317 Basin and surrounding islands. Maps are produced using the open-access QGIS software
318 (<https://www.qgis.org>)

319

320 *3.3 Depth and time calibration of main geological boundaries.*

321 In order to measure offsets of unconformities on time-migrated seismic lines we
322 need to constrain the seismic velocities within the sediments. We used velocities from the
323 WAS profile (Kopp et al., 2011) in the south of Marie-Galante, that trends parallel to the
324 MCS line Agua116 (Cornée et al., 2023). The WAS velocities in the *ca.* 0.4 stwt (second
325 two way time) thick upper unit (MG-MS3 – Cornée et al., 2023) ranges between 2 and 2.5
326 km/s. The 3.25 km/s isochrones mimic the base of unit MG-MS2 and the 4.5 km/s
327 isochrones follow the acoustic basement below MG-MS1. Moreover, KaShallow 2 cruise

328 MCS data (Table 1) acquired with a 600 m long streamer allows us to determine the
329 Normal Move Out velocities down to a depth of *ca.* 0.75 stwt in well-layered units such as
330 shown on the seismic lines (Figure 3). Once converted into interval velocities using the
331 “Hewitt Dix formula”, we determine velocities in the upper unit from 1500 to 2750 m/s
332 (Dix, 1955). Therefore, we use 1500 m/s in the water and 2000 m/s and 2500 m/s in the
333 sediments to estimate (and bound) the depth of unconformities observed on time-
334 migrated seismic lines (Table 2).

335 Offshore, several first order unconformities and sedimentary units were
336 accurately dated using bio-stratigraphy analysis or radiochronology (Bouysse and
337 Mascle, 1994; KaShallow Research Program results: Münch et al., 2013; De Min, 2014;
338 De Min et al., 2015; Cornée et al., 2023). The deepest dated unconformity, MG-SB2, which
339 corresponds to the top of the MG-MS1 sequence, occurs on seismic lines east of Marie-
340 Galante (thick orange line on Figure 5, lines AGUA97 – K09-09 – K09_45 - Sis7C). Along
341 the seismic line Agua 97, the F8 fault scarp has been sampled at 514 m bsl just beneath
342 the unconformity (KaShallow Cruise ROV dive, Figure 6). The samples, BMG2 and 4,
343 yielded a Late Burdigalian/earliest Langhian age (Cornée et al., 2023). Thus, we propose
344 16 Ma \pm 1Ma for the age of MG-SB2. Above, another regional unconformity MG-SB3
345 (Cornée et al., 2023) is identified east of Marie-Galante. It corresponds to the top of MG-
346 MS2 sequence (thick purple line on the Figure 5 lines Agua97 – K09-09-08 – K09-45-44
347 – Sis7C). The age for this surface is bracketed between the overlaying Late Messinian GT
348 carbonate platform (zones N18, 5.8-5.33 Ma –Cornée et al., 2023) and the underlying
349 sedimentary unit dated Late Tortonian 8.57 \pm 0.43 Ma (Ar-Ar, Münch et al., 2014). We
350 thus consider 7 \pm 1.5 Ma for the age of MG-SB3. West of Marie-Galante, the angular
351 unconformity on line K09-90 North-West of Marie-Galante may corresponds to MG-SB3
352 (Figure 4). However, this reflector is too deep to be followed across the whole fault
353 system. Within the uppermost sequence, MG-MS3, a remarkable unit boundary
354 corresponding to a second order unconformity, can be easily correlated throughout the
355 basin and onshore (red thick line on Figure 4). This unit boundary is Middle-Late
356 Piazencian offshore and correlates onshore with the 3–2.9 Ma tectonically-induced
357 erosional unconformity SB1 (see above; Cornée et al., 2023). Along the seismic line
358 Ber03-30-31, the fault scarp immediately north of F3 and F4 has been sampled at 283 m
359 bsl (KaShallow Cruise ROV dive, Figure 4). Samples, BC1 and BC2, yielded ages of 1.33 \pm
360 0.23 Ma and 1.15. \pm 0.12 Ma, respectively (Ar⁴⁰/Ar³⁹ ages on plagioclases, Münch et al.,

361 2013; 2014). These samples correspond to a prominent seismic reflector within the
362 upper unit of MG-MS3 sequence that can also be easily correlated through all the seismic
363 lines west of Marie-Galante. We thus retain an average age of 1.29 ± 0.26 Ma for this
364 seismic reflector (green line on Figure 4).

365

366 *3.4 Tsunami modeling*

367 In order to test the tsunamigenic potential of the fault system proposed herein, a
368 rupture scenarios has been elaborated and is presented hereafter.

369 Numerical simulations of tsunami generation and propagation were carried out
370 using COMCOT software (Cornell Multi-grid Coupled Tsunami: Liu et al., 1998; Wang,
371 2008; Wang and Power, 2011). COMCOT is widely used by the research community and
372 constantly tested notably through various real tsunami cases (e.g. Prasetya et al., 2011;
373 Gusman et al., 2019; Paris et al., 2021; Gusman et al., 2022; Roger et al., 2023). COMCOT
374 uses a modified staggered finite-difference scheme to solve linear and non-linear shallow
375 water equations in either spherical or Cartesian coordinate systems throughout a set of
376 nested grids allowing refinement of the bathymetric resolution in coastal areas. A two-
377 way nested grid configuration is implemented in the model to balance computational
378 efficiency and numerical accuracy (Wang 2008; Wang and Power 2011).

379 For this study, nesting has been used with two grid levels: the first grid is a 0.5
380 arcmin (~ 900 m) resolution grid of the Lesser Antilles (extent: 295°E , 302°E , 12°S , 18°S)
381 built from the global dataset GEBCO 2021 (GEBCO Compilation Group, 2021); the second
382 grid is a 3.75 arcsec (~ 115 m) spatial resolution grid focusing on the Guadeloupe
383 Archipelago and Dominica Island, including the location of the investigated Morne Piton
384 fault system as shown on Figure 1 (extent: 297.92°E , 300.22°E , 14.94°N , 16.717°N). This
385 second grid has been built from different datasets including the aforementioned
386 bathymetric data (§ 3.2). The highest resolution and the most recent data have been kept
387 first. Data gaps have been filled in with data from GEBCO (GEBCO Compilation Group,
388 2021) for offshore regions, and SRTM version 3.0 Global 1 arcsec data (NASA SRTM,
389 2013) for onshore regions. Continuity of the different datasets has been ensured using
390 kriging interpolation, which has proven to be one of the best methods to produce a well-
391 defined DEM, especially for smooth transitions between different resolution areas (e.g.
392 Bernardes et al., 2006; Arun, 2013; Ajvazi and Czimber, 2019). Note that Dominica was
393 included in the second grid in order to look at potential effects which could occur between

394 the different islands and also to assess the potential tsunami threat resulting from the
395 Morne Piton scenario on this neighboring island.

396 The initial sea-bottom displacement is calculated by COMCOT considering an
397 instantaneous rupture of the fault using the surface deformation model of Okada (1985),
398 and transmission of the deformation to the water column above is considered
399 instantaneous. Calculations of wave propagation have been done at mean sea level (MSL)
400 assuming a constant Manning's roughness coefficient of 0.011 for the seabed friction
401 (Wang et al., 2017). A higher friction coefficient leads to more energy dissipation of
402 tsunami waves, especially in shallow waters, slowing down their speed and reducing
403 their amplitude and impact (e.g. Dao and Tkalich, 2007). Considering the limited extent
404 of the interest zone (~250km x 200km), the rupture parameters (leading to a small
405 coseismic rupture) and the objective to look at potential localized effect as inter-islands
406 resonance, tsunami waves propagation time was set to 10 hours.

407

408 **4. RESULTS**

409

410 *4.1 The Morne Piton fault system*

411 The HR bathymetric data presented here above (section 3.2) allows to refine the
412 structural pattern of the Morne Piton fault system, especially offshore (Figures 3A - B).
413 The fault system splays eastward from the N120-N135°E trending Eastern Les Saintes
414 fault system located east-south-east of Basse-Terre to the N110-115°E trending Petite-
415 Terre fault system south-south-east of Grande-Terre (Figures 2 and 3). Thus, the fault
416 zone spreads over a 5-8 km wide and 50 km long zone with an average N100°E trend.

417 Morpho-bathymetric analysis allows us to identify surficial segments of the faults
418 that are reaching out the seafloor. The main fault scarp of the Morne Piton fault system is
419 the southernmost one, along which 11 fault segments of 1-10 km length can be identified
420 (Figure 3B). From west to east, the F1 segment trends N110° and then the fault steps left
421 along the N75°E trending F2 segment. A little farther east, the fault cuts the northern
422 Colombie Bank and the eastern Marie-Galante platform along closely spaced N90E
423 trending left or right stepping segments F3, F3', F4 and F5. Across the island, the F6
424 segment is a N130°N trending, 6 km long right step relay linking the F5 segment to the F7
425 N90°E trending one. Further east offshore Marie-Galante, two N80°E trending fault
426 segments, F8, 9, 10 and 11, arrange as overlap right steps. There, the fault scarp vanishes

427 in just a few kilometers. To the east of the line Sis7C, neither the sediments nor the
428 basement are affected by the north-dipping Morne Piton fault system (Figure 5). In
429 contrast, the seismic line Sis7C shows that the basement is southwardly downthrown by
430 the Petite-Terre fault system, along south dipping active and sealed faults to the north
431 and south of the Morne Piton fault system, respectively (Figure 5 location on Figure 3A) .
432 West of Marie-Galante, the Morne Piton fault system widens as closely spaced fault splays
433 trending N95°E to N100°E link the main fault scarp (F2, F3 and F4) to the antithetic
434 Goyave Fault system or die westward (Figure 4 location on Figure 3A). Eastward of the
435 F6 segment, some synthetic and a few antithetic faults splay northeastward and link with
436 the N110-115°E Petite-Terre Fault system.

437 The mean fault-scarp height west of Marie-Galante Island is ca. 100 m (Figure 3C).
438 Across Marie-Galante Island, the mean fault-scarp height reaches 200 m and controls the
439 staircase morphology of the island. East of the island, the Marie-Galante Canyon carved
440 the sedimentary units, clearing some of the fault planes increasing their apparent scarps
441 heights up to 400 m. To the east, the canyon meanders and cuts through the eastern tip
442 of the Morne Piton fault system (Figure 3 B and C). West of the island, at the vicinity of
443 the volcanic island of Basse-Terre, either recent deposits or the uppermost sedimentary
444 units seal most of the faults. These observations seem to indicate that the sedimentary
445 rate west of Marie-Galante and the erosional rate east of Marie-Galante (in the canyon)
446 exceed the vertical slip rate of the fault.

447 4.2 Vertical slip rate estimates along the Morne Piton fault system

448 To assess the average vertical slip rate along the Morne Piton fault system, we
449 estimated the fault offset of key dated reflectors across the entire length of the fault
450 system (Figures 4 and 5 – Table 2). West of Marie-Galante, the main offset of the $1.29 \pm$
451 0.26 Ma seismic reflector (green on Figure 4) increases from west to east (i.e., from the
452 westernmost extremity of the fault toward its center). Close to the eastern shore of Basse-
453 Terre Island (Figure 4, profile K09-96, and Table 1), the 1.29 Ma reflector is downthrown
454 by 110-115 m. Eastward, the reflector offset increases up to 230-257 m (Figure 4, line
455 K09-90, K08_24 and Table 2) and reaches a maximum of 300-322 m (Figure 4, lines
456 ber03_30-31, K08-59). Accordingly, the number of sealed structures across the fault
457 system decreases eastward (Figures 3 and 4). Thus, West of Marie-Galante, the Morne

458 Piton fault system accommodates a vertical slip rate increasing eastward up to $0.25 \pm$
459 $0.08 \text{ mm}\cdot\text{yr}^{-1}$ over the last $1.29 \pm 0.26 \text{ Ma}$ (Table 2).

460 The $2.95 \pm 0.05 \text{ Ma}$ Unit Boundary (red line on figure 4) can only be correlated
461 across the fault system along the K08-59 seismic line. Growth strata are observed in the
462 deposits above the 2.95 Ma unit boundary (Figure 4, gray shadow on seismic lines),
463 attesting for syn-sedimentary fault activity. This unit boundary offset reaches 550-620 m,
464 leading to $0.20 \pm 0.02 \text{ mm}\cdot\text{yr}^{-1}$ average vertical slip rate over the last $2.95 \pm 0.05 \text{ Ma}$, i.e
465 ca. $0,16 \text{ mm}\cdot\text{yr}^{-1}$ for the period $2,95 - 1,29\text{Ma}$ (Table 2). West of Marie-Galante Island,
466 deeper reflectors cannot be identified and correlated across the fault system because of
467 the limited seismic penetration.

468 However, east of Marie-Galante, the MG-SB2 sequence boundary dated to $16 \pm$
469 1Ma (orange in Figure 5 – see also Figure 5 in Cornée et al., 2023) is the only reflector
470 that can be correlated on both sides of the fault system. In the hanging wall of the fault,
471 the younger MG-SB3 $7 \pm 1.5\text{Ma}$ boundary (Purple in Figure 5) as well as a large part of
472 the fault scarp are eroded by the Marie-Galante Canyon. The seismic line K09-09 (Figure
473 5) shows that the MG-SB3 unconformity records the Morne Piton fault inception: in the
474 footwall of the fault, the stratigraphy of MG-MS2 sequence (comprised between MG-SB2
475 and MG-SB3) shows conformal deposits flexed upward while approaching the fault,
476 whereas MG-MS3 deposits onlap onto MG-SB3 and present clear growth strata. We thus
477 propose that the $16 \pm 1 \text{ Ma}$ sequence boundary is pre-tectonic and is tilted by the fault
478 since its inception $7 \pm 1.5 \text{ Ma}$ ago (the age of MG-SB3; Figure 5, profile K09-45-45). Along
479 the fault system East of Marie-Galante we calculated the strain rate from MG-SB2 offset
480 since $7\pm 1\text{Ma}$. From east to west the slip rate ranges from $0.067\pm 0.03 \text{ mm}\cdot\text{yr}^{-1}$ at the
481 K09_44-45 seismic line, to $0.071\pm 0.02 \text{ mm}\cdot\text{yr}^{-1}$ along the K09_08-09 line. Seismic line
482 Agua97 (Figure 5) presents the greatest offset of MG-SB2. However, this seismic line does
483 not cross the southernmost F7 segment (the water depth is too shallow for ship
484 navigation in the footwall compartment). We estimated the depth of MG-SB2 in the
485 footwall compartment from the closest seismic line available that crosses the fault located
486 1 km east of the Agua97 line. We obtain an offset of 830-860 m leading to a maximum
487 average vertical slip rate of $0.12 \pm 0.03 \text{ mm}\cdot\text{yr}^{-1}$ since $7 \pm 1.5 \text{ Ma}$, i.e ca. $0,07 \text{ mm}\cdot\text{yr}^{-1}$ for
488 the period $7 - 2,95\text{Ma}$ (Table 2). Consequently, we propose that i) the vertical slip rate
489 accommodated by the Morne Piton fault system increases progressively from each
490 extremity of the fault toward its center, and ii) that the Morne Piton fault system is

491 characterized by an increasing slip rate from *ca.* 0.07 from its inception (*i.e.* 7 Ma ago) to
492 *ca.* 0.25 mm·yr⁻¹ since 1.29 Ma (Table 2).

493 *4.3 Earthquakes parameters of Tsunami modeling*

494 ROV dive along the ber03_30-32 seismic line allowed observation of one of the main
495 morphologic scarps of the Morne Piton fault system across the F2 and F3' segments
496 (Figures 3 and 6). Across the upper plateau, between F2 and F3', we observed several
497 N90°E trending fractures parallel to the fault segments (Figure 6A). While descending
498 across the F3' scarp, the slope progressively steepens up from 45° at 157 m bsl to more
499 than 80° at 280 m bsl just a few meters above the toe of the scarp (Figure 6A, B and C).
500 This morphology suggests a *ca.* 128 m-high cumulative scarp for the F3' segment at that
501 location. The very last meter of the fault scarp above the toe of the slope presents a 100
502 cm-high polished vertical surface, partly altered, showing dip-slip striations indicating
503 pure normal motion along this fault segment (Figure 5D E and F). This exposed and partly
504 altered fault slip plane breaches the sea floor at high angle. Such a polished striated fault
505 scarp morphology is similar, although more altered, to the co-seismic fault scarp
506 observed at the toe of the Roseau Fault plane, after the Les Saintes earthquake (Escartin
507 et al., 2016). We conclude that this observation of the Morne Piton polished striated scarp
508 may correspond to one of the last co-seismic scarps formed during a major earthquake
509 (including possible post-seismic slip motion) along this fault. Alteration of the fault slip
510 plane suggests that the slip event occurred tens to several hundred years ago, *i.e.*, this
511 fault slip plane may correspond to a pre-instrumental earthquake (see discussion). From
512 this observed scarp we obtained a ratio of last event scarp over total scarp height (proxy
513 for the cumulative slip as determined on Figure 3) of ~2,6%. With this ratio we calculated
514 an average scarp of ~75 cm along the whole length of the fault and a maximum scarp of 2
515 m. Such an average scarp value corresponds to the surface expression of a magnitude M_w
516 ~6.7 earthquake using the criteria of Wells and Coppersmith (1994), or even 7 according
517 to Thingbaijam et al. (2017). The same studies also provide a calculated maximum
518 displacement of ~2m, consistent with the maximum observation along the scarp.
519 Moreover, the 45 km total length of the Morne Piton fault system measured from HR
520 bathymetry, together with the width of the fault given by the 10 to 15 km thick
521 seismogenic crust, lead to a rupture area ranging between ~ 450 to 675 km² that would
522 generate a magnitude M_w ~6.7 ± 0.1 earthquake corroborating the afore range of

523 magnitude deduced with other observations (e.g., M_w ranging between 6.6 and 6.8
524 according Wells and Coppersmith, (1994) and Leonard (2010) and around 7 according
525 to Thingbaijam et al., 2017). The rupture parameters for the different identified segments
526 of the fault shown on figure 3B are provided in Table 3. Geographic location of the center
527 of top of the fault plane and azimuth are provided based on our structural analysis
528 (section 4.1 and 4.3). Neither seismic lines which illustrate only a few hundred of meters
529 nor in-depth earthquake distributions (which is not enough resolved) allow to estimate
530 the dip of the Morne Piton fault system. Thus, after considering the influence of dip on
531 surface deformation which turns out to be negligible, we choose a mean dip of 75° for the
532 fault segments after Feuillet et al. (2004). The shape of the rupture area (along-strike
533 length x downdip width) and a slip of 1.89 m (maximum displacement estimated from
534 scarp heigh measurement) is implemented for each segment in order to fit with a total
535 fault surface of ca. 500 km^2 , corresponding to a magnitude M_w 6.5 earthquake. Finally,
536 conformably to pure dip slip striations observed along the F3' segment (section 4.3) and
537 the F7 segment (Feuillet et al. 2002), we apply a rake of 90° , corresponding to a pure
538 normal faulting mechanism as observed by Feuillet et al. (2004) at Anse Piton and by the
539 ROV picture of the present study. Fault segments F8 and F9 are not straight, for the
540 purpose of modeling they have been divided into F8-F9 and F10-F11 (Figure 7).
541 Hereafter, we use these parameters to evaluate the potential tsunami hazard from the
542 Morne Piton fault for a worst-case plausible scenario rupturing all the segments
543 simultaneously.

544

545 *4.4 Plausible worst-case tsunami scenario and resulting hazard*

546 We present a worst-case plausible scenario, related to a rupture along all the
547 identified segments of the Morne Piton fault system as these 1 to 10 km-long segments
548 most probably root in-depth along a single fault zone (Feuillet et al., 2004). We rule out
549 the eventuality of testing a single 10 km-long segment of the Morne Piton fault system
550 rupture as it would generate a $M_w < 6.0$ earthquake and would thus unlikely consist in a
551 tsunami source (e.g., Roger et al., 2019). Here, we use a plausible M_w 6.5 scenario, i.e a
552 magnitude slightly lower that the maximum magnitude M_w 6.7 deduced from the
553 morphological analysis, but close enough to the Les Saintes earthquakes magnitude as
554 both Les Saintes and Morne Piton fault systems share close morphological characteristics.
555 Our model would generate a tsunami with a significant energy/amplitude to accurately

556 highlight the potential consequences of tsunami waves' propagation and interaction with
557 the peculiar shallow reliefs and major embayment located in and around the Marie-
558 Galante Basin. Quantifying horizontal run-up at the coast and assessing tsunami risk
559 following a rupture along this fault is out of the scope of the present study as such
560 quantifications necessitate a better knowledge of the fault dynamic itself (return period
561 of large events, etc.).

562 The initial surface elevation directly resulting from the Okada (1985)'s formulation is
563 presented in Figure 7. Due to the high inclination of the fault planes (dip = 75°) dipping
564 globally northward, a profile cut of the initial displacement is represented from the north
565 to the south by a crest (positive elevation) and a trough (negative elevation). At t=0, the
566 shallow water equations take over from this initial deformation and the propagation of
567 the tsunami waves is calculated over the nested grids at adequate time steps. Figure 8
568 presents the state of the virtual water surface at six different times of the tsunami waves
569 propagation from 1 to 16 minutes. The wave front initially parallel to the fault axes (t ≤ 1
570 min) is progressively influenced by the bathymetry within the very first minutes
571 following the rupture, leading to an anisotropic propagation of the waves showing
572 variability in space and time. In addition, the fact that the fault literally crosses Marie-
573 Galante leads to the tsunami source being divided in two independent sources located on
574 the west and east of this island: two tsunamis are therefore generated and called TsuW
575 (on the west) and TsuE (on the east) hereafter. These two tsunamis propagate from their
576 origin and wrap around Marie-Galante as shown at t=4 min of propagation. Then,
577 between 4 and 9 min, the two tsunami fronts meet on the north and south of Marie-
578 Galante. Meanwhile, the propagation of the TsuW waves meet the shallow waters of the
579 Banc Colombie shoal (approx. coordinates: 15.98°N/-61.43°W; minimum water depth is
580 about 35m), west of Marie-Galante: the waves' amplitude increases as they slow down
581 and their interaction leads to a constructive interference resulting in a "new" tsunami
582 source at the Banc Colombie shoal, mainly showing a negative wave propagating
583 southward with some extensions toward Marie-Galante on the east and Les Saintes on
584 the west.

585 Approaching the coasts, wave shoaling takes over, the reduction in water depth
586 slowing down the waves and simultaneously increasing their amplitude. It leads to wave
587 amplification as particularly shown along Marie-Galante north shore, the southeast coast
588 of Basse-Terre and the south of Petite-Terre and eastern Grande-Terre (Figure 9).

589 After 10 hours of tsunami propagation, the maximum values of wave amplitude
590 reached on each point of the simulation domain are shown in Figure 9. The overall impact
591 of such an event is that the maximum wave amplitude is not going over 1.2 m, carefully
592 considering the 100 m resolution of the simulation domain: in fact, grid refinement at the
593 coast showing higher resolution would probably highlight higher wave amplitude in very
594 localized areas because of interaction with small underwater structures not represented
595 at this resolution, as well as non-linear effects. The patterns of those amplitudes indicate
596 that not only the fault region but also some coastal regions are exposed to tsunami waves
597 of 50 cm or more, which is above the usual beach and marine threat 30-cm threshold. It
598 is the case for the neighboring coasts of Marie-Galante, southeast Basse-Terre, south
599 Grande-Terre and the natural reserve of Petite-Terre. The southeast coast of Basse-Terre
600 is particularly exposed with wave amplitudes of more than 1 m (Figure 9a). A focus on
601 Les Saintes Archipelago highlights also wave amplitudes of more than 1 m, even between
602 the islands (Figure 9b). The northeast coast of Dominica is also affected but to a lesser
603 extent (maximum wave amplitudes of ~50 cm). Further high-resolution simulation,
604 including flow speed calculations, would help to correctly assess the related hazard on
605 this island. Virtual sea-level gauges have been added at different locations of grid 2
606 (Figure 9) in order to check if the model is stable and to look for possible resonance
607 (especially in Les Saintes Archipelago). The raw signal of seven VG (top figure 10)
608 highlights a clear decrease of the amplitude over the time on all stations. However, for
609 stations VG_1, VG_2 and VG_3, a low-frequency oscillation is clearly visible and lasts for
610 at least 10 hours. The amplitude spectrums on these three stations show that two peaks
611 with a period of ~8.5 min and 15 min respectively are present on the three signals at Les
612 Saintes, which is not the case for the stations out of the archipelago. Moreover, the high
613 amplitude negative wave southwardly propagating generated by the “new” tsunami
614 source at the Banc Colombie shoal, is shown by VG_1 on figure 10 with a peak to trough
615 value of ~0.6 m. VG_2 and VG_3 also show it to a lesser extent a bit later.

616

617 **5. Discussion**

618

619 *5.1. Upper plate fault tsunamigenic potential.*

620 Les Saintes earthquake demonstrated that upper plate normal faults may generate
621 $M_w > 6$ tsunamigenic earthquakes in the Lesser Antilles. Les Saintes tsunami produced up

622 to 2 m high waves at the coast and 42 m distance run-up in a peculiar embayment (Zahibo
623 et al. 2005). Such normal faults are prone to be tsunamigenic because their rupture is
624 relatively shallow (compared to the megathrust), and their slip motion is favorable to
625 large seafloor displacement. Together with their proximity to the islands, they are able to
626 produce metric-high tsunami waves at the coast and tens to hundreds of meters of run
627 up distances (depending on the topography). Therefore, upper plate crustal faults may
628 represent a major potential tsunami hazard in the Lesser Antilles islands and particularly
629 in the Guadeloupe Archipelago as pointed out by the Intergovernmental Oceanographic
630 Commission held in Fort-de-France in 2019 (IOC-UNESCO, 2020). Similarly to Les Saintes
631 Fault, we assume that the 50 km long Morne Piton fault poses a potential earthquake and
632 tsunami hazard. The large scarp we observed at the toe of the Morne Piton fault suggests
633 recent seismogenic rupture(s) along this structure, potentially tsunamigenic. However,
634 this scarp might not be related to the 1851 historical event as the estimated magnitude
635 M_w 5-5.5 for this earthquake appears too low to explain the observed scarp. Thus, a
636 rupture of the fault along its whole length must not be excluded. Several other prominent
637 onshore-offshore faults affect the seafloor and the topography of the archipelago and may
638 represent both an earthquake and a tsunami hazard. However, the relationships between
639 faults, earthquakes and tsunami is not clearly established as shown in the following
640 examples.

641 Along the arc, the Harvers-Montserrat-Bouillante and Les Saintes fault systems are
642 the most prominent tectonic features (Feuillet et al., 2010). To the south, Les Saintes Fault
643 system dips east and defines a half-graben (Leclerc et al., 2016). The westernmost fault,
644 the Roseau fault, ruptured during the 2004 M_w 6.3 earthquake and is most likely
645 reloading stress and therefore quiet. Recurrence time for this earthquake has been
646 estimated to be more than 1,000 years given the regional slow strain rate. However, the
647 eastern normal faults of the system offset the seafloor over more than 30 km and present
648 tilted blocks filled by fan shaped late Pleistocene deposits attesting for recent
649 deformation. In the light of these observations, the eventuality of a tsunamigenic
650 earthquake along these faults should be considered. To the North-West along the Harvers
651 segment, a rupture occurred in 1985 with a M_w 6.5 earthquake showing strike-slip
652 mechanisms. Beck et al., (2012) estimated a recurrence time of 6,500-7,000 years for
653 such a M_w 6.5 event based on the vertical offset of coseismic deposits in hemipelagites
654 imaged by very high-resolution seismic lines across the fault. In between these two

655 segments, the Montserrat-Bouillante segment is seismically quiet except if the 1897
656 (estimated M_w 7.0) earthquake occurred along this fault (Feuillet et al., 2011b). However,
657 no tsunami related to such a rupture has been reported. Seismic lines across the
658 Montserrat-Bouillante fault (Feuillet et al., 2010; Legendre, 2018) reveal that the fault
659 offsets the most recent units including the oldest reflector drilled during the IODP1395,
660 that dates upper Gelasian *ca.* 1.8-2Ma (Le Friant et al. 2013). Given an offset of 0.3m stwt
661 and a 2000-2500 m/s sediments velocity this provides a 0.15-0.2 $\text{mm}\cdot\text{yr}^{-1}$ slip rate. Thus,
662 the Montserrat-Bouillante segment should also be considered tsunamigenic (Figure 2).

663 South of Grande-Terre of Guadeloupe, the N90°E trending Gosier Fault system
664 bounds 45 km of coastal area (Figure 2). The fault system offset the Mid-Pleistocene
665 Grande-Terre plateau that culminates at +150 m from the offshore plateau that rests 15-
666 20 mbsl (Münch et al., 2013). This suggests a long-term vertical slip rate *ca.* 0.10 $\text{mm}\cdot\text{yr}^{-1}$
667 ¹. To the east of Grande-Terre, the fault crosscuts the MIS5e terrace attesting for Late
668 Pleistocene activity of the fault. However, evaluation of paleo-seismicity along one
669 eastern segment of the fault system by the means of trenches allowed the identification
670 of recent surface ruptures, although superficial deposits remain undated (Terrier and
671 Combes, 2002).

672 East of Guadeloupe, offshore, the Marie-Galante Basin is bounded to the east by
673 the Karukera spur (Figure 2D), a 75 km long N-S trending submerged plateau that
674 culminates 30 mbsl to the north offshore La Désirade Island, and gently dips southward
675 down to *ca.* 1500 mbsl (De Min et al., 2015). The spur is bounded to the west by N150°E
676 to N0°E trending, west dipping, and normal faults. These faults offset the middle Miocene
677 sequence boundary (SB2) by up to *ca.* 2,700-2,900 m, leading to a long-term vertical slip
678 rate of 0.16-0.18 $\text{mm}\cdot\text{yr}^{-1}$. Recent deposits are clearly affected by tectonic activity (Siebert
679 et al., 2020). Located far from the islands, the earthquake intensity felt onshore would be
680 relatively low in the island, but a tsunami could propagate across the Marie-Galante Basin
681 directly toward the coasts of the Lesser Antilles Arc islands.

682

683 *5.2. Slip rate reassessment along the Morne Piton fault system*

684 With this study, we evidence that the slip rate along the Morne Piton fault system
685 increases through time with a maximum slip rate of $0.25 \pm 0,08 \text{ mm}\cdot\text{yr}^{-1}$ since the last 1.29
686 Ma. This slip rate is up to four times slower than previous estimates. Over the last 330 Ka,
687 Feuillet et al. (2004) estimate a bulk slip rate along the Morne Piton fault as high as 1

688 mm·yr⁻¹ over 330 – 125 Ka then decreasing to 0.3 mm·yr⁻¹ since the last 125 Ka. This last
689 value is close to the long-term slip rate obtained offshore in this study (Figure 11). These
690 results suggest that the fault may present a fast slip rate during short periods of time (few
691 100 ka.) separated by long periods (million years) of low slip rate. The fast 1 mm·yr⁻¹ rate
692 was obtained considering that the terrace T2MG is offset by the fault by 159 m and dates
693 MIS7e (249 Ka) and the upper-plateau of Marie-Galante corresponds to an abrasion
694 surface from the MIS9e high stand (330 Ka) (Feuillet et al., 2004).
695 This latter statement can be reconsidered. The same *Agaricia sp.* limestone unit, and
696 *Acropora sp.* limestone unit top the three islands, Grande-Terre – La Désirade – Marie
697 Galante, suggesting they emerged synchronously (Feuillet et al., 2002; Cornée et al., 2012;
698 Munch et al., 2013). In the 3 islands the youngest formation, *Acropora* unit, is not younger
699 than 1.07 Ma and not older than 1.54Ma (Cornée et al., 2012; Münch et al., 2014). From
700 the geological map of Bouysse et al. (1993), this unit rims Marie-Galante Island. In La
701 Désirade, the Upper Plateau culminates at 276 m asl (above sea level), whereas the 330
702 Ka terrace is at 35 m asl (Lardeaux et al., 2014; Leticée et al., 2019). Consequently, the
703 hypothesis stating that the plateau emerged 330 Ka ago can be ruled out in Marie-Galante.
704 Based on the age of the latest deposit of the Marie-Galante Plateau that range between
705 1.54 and 1.07 Ma, a vertical slip rate of 0.15-0.22 mm·yr⁻¹ can be calculated. This value is
706 close to the ca. 0.25 mm·yr⁻¹ obtained offshore for the slip rate along the Morne Piton
707 fault system over the same period of time (Figure 11). As a consequence, it is not possible
708 to conclude that the Morne Piton fault system has short periods of fast slip rate, but
709 instead it probably increases through time, a reaching a maximum slip rate of 0.25 mm·yr⁻¹
710 over the last million years. As a consequence, dividing by four the slip rate along the
711 Morne Piton fault system is increasing the earthquake time recurrence along this fault
712 system and thus the time recurrence of potential associated tsunami. Constraining the
713 fault slip rate at the time scale of one or few seismic cycles may allow better estimates of
714 seismic and tsunamigenic hazards of the Morne Piton fault system. This would require a
715 better knowledge of in-depth fault geometry and identification of its active segments that
716 could be obtained by the means of a microseismic survey (using Ocean Bottom
717 Seismometers acquisition over 1-2 years or more). At present-day, BOTDR laser
718 reflectometry is used to perform long-term monitoring of the Morne Piton fault using the
719 network of submarine telecom fiber optic cables connecting Marie-Galante to the larger
720 islands of Basse-Terre and Grande-Terre (Gutscher et al., 2023). It is to note that given

721 the slow strain rate and in the absence of rupture occurring along the fault during the
722 survey period, identifying slip rate across this fault system may require hundreds to
723 thousands of years. Moreover, very high-resolution seismic data across the fault in areas
724 of high sedimentation rates (*i.e.*, along the eastern coast of Basse-Terre Island) may
725 constrain the Holocene fault activity. Slip rate estimates can be obtained by coring and
726 dating of (i) the most recent deformed sediments as well as (ii) tsunami deposits in salt
727 marshes. Finally, such regional monitoring would also contribute to a survey of past and
728 potential landslides that may also be induced by earthquakes and which may locally
729 generate destructive waves.

730

731 *5.3. Bathymetric features control on tsunami wave propagation*

732 The aim of the tsunami simulation associated to the present study is not to
733 produce a precise hazard assessment for the islands of Guadeloupe, but rather to give an
734 overview of what could happen in terms of tsunami generation if all the identified
735 segments of the Morne Piton fault system ruptured together, and to identify a few gaps in
736 terms of scientific knowledge and operational activities. An accurate hazard assessment
737 study would require many rupture scenarii including combinations of the segments used
738 in this study, with variations of their parameters and sensitivity tests.

739 The main outcome of the simulation presented above lies in the fact that
740 submarine features play an important role on the tsunami waves behavior and amplitude.
741 Submarine canyons are known to focus the waves (e.g.: along the continental slope of the
742 middle American trench: Álvarez-Gómez et al., 2012; or at Nazarè Portugal: Martins et
743 al., 2010; do Carmo et al., 2022; Delpy et al., 2021). This behavior also occurs along the
744 rime of the island submarine plateau rising the wave amplitude as exemplified in front of
745 the most populated cities of south-eastern Grande-Terre (Figure 9). Shallow water
746 plateaus located around or between islands slow down the waves which leads to
747 particular propagation patterns like the wrapping around the relief (Figure 8). There, the
748 wrapping effect of the waves around Marie-Galante and the Colombie Bank results in two
749 distinct tsunami sources, *i.e.* a primary source at fault and a secondary one at the
750 Colombie Bank (Figure 8). Such a behavior, already shown in other regions, is able to
751 considerably amplify the impact of the tsunami on the coast opposite to the fault rupture
752 (Chadha et al., 2005; Chen et al., 2010). It is important to notice that the low resolution of
753 the grid used for the present simulations is a limiting factor in quantifying correctly the

754 wave amplitude along the shoreline. A higher resolution simulation grid would better
755 reproduce the bathymetric features, especially in shallow waters, having a non-negligible
756 impact on the waves' behavior and amplitude.

757 Our simulation also highlights interesting phenomena that would require further
758 consideration in the framework of further tsunami hazard studies: wave oscillation,
759 which could be attributed to a resonance effect, is clearly visible within the Les Saintes
760 Archipelago, and potential wave trapping is also visible around those islands. If the
761 second case is purely observation, the resonance between Les Saintes islands is clearly
762 revealed by the single-sided Fourier amplitude spectrum (Figure 10) and the peak at ~15
763 min seems to be associated with the negative wave coming time after the initial wave
764 front and related to the tsunami interaction with the Colombie Bank shoal. The records
765 provided by the virtual gauges located beforehand within the archipelago (VG_1, VG_2 &
766 VG_3) clearly shows a long-period oscillation of the signal which is not present on the
767 gauges located outside of Les Saintes (VG_4, VG_5, VG_6 & VG_11). It shows how the
768 frequency content of the incoming signal can affect the sea-level during many hours after
769 the seismic rupture.

770 The numerical simulations performed by Cordrie et al. (2020) of the tsunami
771 having followed the M_w 6.3 Les Saintes earthquake were able to match the witnesses'
772 observations in Les Saintes (Zahibo et al., 2005). Despite the low resolution (100m) of the
773 present simulation on Les Saintes, there are some similarities between the two studies of
774 potential impacted zones, for example in Marigot or Grande Anse Bays. It also shows that
775 other bays, like the ones located between Terre-de-Haut and Ilet à Cabrit, appear to be
776 quite well protected and not exposed to relatively strong tsunami waves.

777 Finally, this study also highlights the exposed coastline of Dominica: on the north-
778 northeast coast of the island (Figure 9), 50+ cm waves are simulated, showing that this
779 island should integrate such a scenario of crustal fault rupture within its tsunami hazard
780 assessment plan.

781

782 ***Conclusions***

783

784 Thanks to HR bathymetry, reflection seismic data and rock/sediment samples, the
785 analyses of the morphology and tectonic structures of the Marie Galante Basin located in
786 the middle of the Guadeloupe Archipelago, allow to detail the structural pattern of this

787 region and to estimate a slip rate of *ca.* 0.1 mm·yr⁻¹ increasing over the last million year
788 to 0.25 mm·yr⁻¹, along the Morne Piton fault system, , cross-cutting the basin. This
789 estimate divides the previously published estimations of the slip rate by four, and thus
790 increases the earthquake recurrence time associated to the Morne Piton fault system
791 from 1Ka to 4-5 Ka. We show that a seismic rupture associated to an earthquake showing
792 a moment magnitude $M_w \sim 6.5$ can occur along the Morne Piton fault system in case of the
793 rupture of the full length of the fault (all segments being considered connected at depth
794 in the present demonstration). Such an event would be tsunamigenic according to
795 numerical simulation results. The multi-segment tsunami modeling illustrates how
796 submarine morphological and structural features influences the propagation pattern of
797 the tsunami leading to constructive interferences and resonances, thus increasing the
798 tsunami threat on nearby islands, especially highlighting a resonance effect within the
799 Les Saintes Islands, not discussed so far (and potentially the explanation of the so-far
800 unreproduced run-up values of the 2004 tsunami). At a regional scale we evidenced that
801 several other regional faults such as Montserrat-Harvers-Bouillante Fault, Gosier Fault,
802 Karukera Spur Border Fault, may also be tsunamigenic. Indeed, although they have the
803 potential to produce relatively low magnitude (<7) earthquakes, their rupture could
804 occur at shallow depth and close to a highly populated coast. Therefore, scenarii with arc
805 and forearc crustal fault ruptures must be integrated within their tsunami hazard
806 assessment plan. For that, it is necessary to have a better knowledge of onshore-offshore
807 structural and seismogenic patterns of each individual major faults system as the regional
808 low strain rate leads to large recurrence time of tsunamigenic earthquakes (> 1,000
809 years), *i.e.* much greater than the historical record. In addition, these earthquakes could
810 also have the capacity to destabilize the sedimentary layers at the edge of plateaus and
811 canyons, triggering submarine mass failures, capable of triggering large but more
812 localized tsunamis.

813

814 ***Competing interests***

815

816 The contact author has declared that none of the authors has any competing interests.

817

818 ***Acknowledgements and data***

819

820 We are grateful to C. Deplus, A. Hirn (IPGP) and M. Laigle (GeoAzur) for providing
821 Aguadomar and Sismantilles seismic and bathymetry data and to I Thinon and P. Gennoc
822 (BRGM) for providing the Geoberyx seismic data. The Kashallow project was supported
823 by The French National Program DyETI from INSU-CNRS, by the European Interreg IIB
824 “Caribbean Space” Fund engaged in Guadeloupe with the EFRD projects (op. 30-700) and
825 the Region Guadeloupe. Part of this study was funded by the New Zealand’s Strategic
826 Science Investment Fund (SSIF).

827

828 ***Data availability and request***

829

830 Litto3D data can be found at <https://diffusion.shom.fr/loisir/litto3d-guad2016.html>
831 French oceanographic fleet data can be obtain on demand via the Simer online interface
832 following the cruise doi – Aguadomar: <https://doi.org/10.17600/98010120>; Sismantilles:
833 <https://doi.org/10.17600/1080060> and <https://doi.org/10.17600/7010020>; Kashallow:
834 <https://doi.org/10.17600/9020010>;

835 Requests for the Geoberyx03 data must be addressed to the BRGM.

836 Some figures have been prepared using the Generic Mapping Tools Version 6 software
837 (Wessel et al., 2019).

838

839

840

841 **References**

- 842
- 843 Accary, F., & Roger, J., 2010. Tsunami catalog and vulnerability of Martinique (Lesser Antilles,
844 France). *Science of Tsunami Hazards*, 29(3).
- 845 Ajvazi, B., & Czimber, K., 2019. A comparative analysis of different DEM interpolation methods in
846 GIS: case study of Rahovec, Kosovo. *Geodesy and cartography*, 45(1), 43-48.
847 <https://doi.org/10.3846/gac.2019.7921>
- 848 Arun, P.V., 2013. A comparative analysis of different DEM interpolation methods. *The Egyptian,*
849 *Journal of Remote Sensing and Space Science*, 16(2), 133-139.
850 <https://doi.org/10.1016/j.ejrs.2013.09.001>
- 851 Barkan, R. and Ten Brink, U., 2010. Tsunami simulations of the 1867 virgin island earthquake:
852 Constraints on epicenter location and fault parameterstsunami simulations of the 1867
853 virgin island earthquake: Constraints on epicenter location. *Bulletin of the Seismological*
854 *Society of America*, 100(3), pp.995-1009. <https://doi.org/10.1785/0120090211>
- 855 Bazin, S., Feuillet, N., Duclos, C., Crawford, W., Nercessian, A., Bengoubou-Valerius, M., ... & Singh,
856 S. C., 2010. The 2004–2005 Les Saintes (French West Indies) seismic aftershock sequence
857 observed with ocean bottom seismometers. *Tectonophysics*, 489(1-4), 91-103.
858 <https://doi.org/10.1016/j.tecto.2010.04.005>
- 859 Beck, C., Reyss, J.L., Leclerc, F., Moreno, E., Feuillet, N., Barrier, L., Beauducel, F., Boudon, G.,
860 Clément, V., Deplus, C. and Gallou, N., 2012. Identification of deep subaqueous co-seismic
861 scarps through specific coeval sedimentation in Lesser Antilles: implication for seismic
862 hazard. *Natural Hazards and Earth System Sciences*, 12(5), pp.1755-1767.
863 <https://doi.org/10.5194/nhess-12-1755-2012>
- 864 Bernard, P., & Lambert, J., 1988. Subduction and seismic hazard in the northern Lesser Antilles:
865 Revision of the historical seismicity. *Bulletin of the Seismological Society of America*, 78(6),
866 1965-1983.
- 867 Bernardes, T., Gontijo, I., Andrade, H., Vieira, T.G.C., Alves, H.M.R., 2006. Digital Terrain Models
868 Derived from SRTM Data and Kriging. In: AbdulRaman A., Zlatanova S., Coors V. (eds)
869 Innovations in 3D Geo Information Systems. Lecture Notes in Geoinformation and
870 Cartography. Springer, Berlin, Heidelberg. [https://doi.org/10.1007/978-3-540-36998-](https://doi.org/10.1007/978-3-540-36998-1_51)
871 [1_51](https://doi.org/10.1007/978-3-540-36998-1_51)
- 872 Bie, L., Rietbrock, A., Hicks, S., Allen, R., Blundy, J., Clouard, V., Collier, J., Davidson, J., Garth, T.,
873 Goes, S., Harmon, N., Henstock; T., van Huenen, J., Kendall, M., Krüger, F., Lynch, L.,

874 Macpherson, C., Robertson, R., Tait, S., Wilknison, J. & Wilson, M., 2020. Along-arc
875 heterogeneity in local seismicity across the Lesser Antilles subduction zone from a dense
876 ocean-bottom seismometer network. *Seismological Research Letters*, 91(1), 237-247.
877 <https://doi.org/10.1785/0220190147>

878 Biggs, J., & Wright, T. J., 2020. How satellite InSAR has grown from opportunistic science to
879 routine monitoring over the last decade. *Nature Communications*, 11(1), 1-
880 4.<https://doi.org/10.1038/s41467-020-17587-6>

881 Bilek, S. L. (2010). Invited review paper: Seismicity along the South American subduction zone:
882 Review of large earthquakes, tsunamis, and subduction zone complexity. *Tectonophysics*,
883 495(1-2), 2-14. <https://doi.org/10.1016/j.tecto.2009.02.037>

884 Boucard, M., Marcaillou, B., Lebrun, J. F., Laurencin, M., Klingelhofer, F., Laigle, M., Lallemand, S.,
885 Schenini, L., Graindorge, D., Cornee, J.J., Münch, P. & Philippon, M., 2021. Paleogene V-
886 shaped basins and Neogene subsidence of the Northern Lesser Antilles Forearc. *Tectonics*,
887 40(3), e2020TC006524. <https://doi.org/10.1029/2020TC006524>

888 Bouysse P., Garrabé F., Mauboussin T., Andreieff P., Battistini R., Carlier P., Hinschberger F. &
889 Rodet J. (1993). – Carte géologique du département de la Guadeloupe. Notice explicative:
890 Marie-Galante et îlets de la Petite-Terre, scale 1: 50, 000. – BRGM, Orléans, France.

891 Bouysse, P., Mascle, A. (1994). Sedimentary Basins and Petroleum Plays Around the French
892 Antilles. In: Mascle, A. (eds) *Hydrocarbon and Petroleum Geology of France*. Special
893 Publication of the European Association of Petroleum Geoscientists, vol 4. Springer, Berlin,
894 Heidelberg. https://doi.org/10.1007/978-3-642-78849-9_32.

895 Chadha, R. K., Latha, G., Yeh, H., Peterson, C., & Katada, T. (2005). The tsunami of the great
896 Sumatra earthquake of M 9.0 on 26 December 2004–Impact on the east coast of India.
897 *Current Science*, 1297-1301.

898 Chen, J. M., Liang, D., & Tang, H. (2012). Interaction between tsunami waves and isolated conical
899 islands. *Journal of Coastal Research*, 28(5), 1270-1278.

900 Colon Useche, S., Clouard, V., Ioualalen, M., Audemard, F. and Monfret, T., 2023. Simulation of
901 tsunami inundation for the island of Martinique to nearby large earthquakes. *Bulletin of the*
902 *Seismological Society of America*, 113(1), pp.252-267.
903 <https://doi.org/10.1785/0120220093>

904 Corbeau, J., Feuillet, N., Lejeune, A. M., Fontaine, F. R., Clouard, V., Saurel, J. M., & OVSM team, 2021.
905 A significant increase in interplate seismicity near major historical earthquakes offshore
906 martinique (FWI). *Bulletin of the Seismological Society of America*, 111(6), 3118-3135.
907 <https://doi.org/10.1785/0120200377>

908 Cordrie, L., Gailler, A., Escartin, J., Feuillet, N., & Heinrich, P., 2020. Simulation of the 2004 tsunami
909 of Les Saintes in Guadeloupe (Lesser Antilles) using new source constraints. *Natural*
910 *Hazards*, 103(2), 2103-2129. <https://doi.org/10.1007/s11069-020-04073-x>

911 Cornée, J. J., Leticée, J. L., Münch, P., Quillevere, F., Lebrun, J. F., Moissette, P., Braga, C., Melinte-
912 Dobrinescu, M., De Min, L., Oudet, J. & Randrianasolo, A., 2012. Sedimentology,
913 palaeoenvironments and biostratigraphy of the Pliocene–Pleistocene carbonate platform
914 of Grande-Terre (Guadeloupe, Lesser Antilles forearc). *Sedimentology*, 59(5), 1426-1451.
915 <https://doi.org/10.1111/j.1365-3091.2011.01311.x>

916 Cornée, J. J., Münch, P., Philippon, M., Boudagher-Fadel, M., Quillévéré, F., Melinte-Dobrinescu, M.,
917 Lebrun, J.F., Meyer, S., Montheil, L., Lallemand, S., Marcaillou, B., Laurencin, M., Legndre, L.,
918 Garroq, C., Boucard, M., Beslier, M.O., Laigle, M., Schenini, L., Fabre, P.H. & Marivaux, L.,
919 2021. Lost islands in the northern Lesser Antilles: possible milestones in the Cenozoic
920 dispersal of terrestrial organisms between South-America and the Greater Antilles. *Earth-*
921 *Science Reviews*, 217, 103617. <https://doi.org/10.1016/j.earscirev.2021.103617>

922 Cornée, J.J., De Min, L., Lebrun, J.F., Quillévéré, F., Melinte-Dobrinescu, M., BouDagher-Fadel, M.,
923 Montheil, L. , Marcaillou, B., Thinon, I. and Philippon M., 2023. Paleogeographic evolution
924 and vertical motion of the central Lesser Antilles forearc since the Early Miocene: A
925 potential driver for land fauna dispersals between the americas. *Marine and Petroleum*
926 *Geology*, 152, 106264. <https://doi.org/10.1016/j.marpetgeo.2023.106264>

927 Dao, M. H., & Tkalich, P., 2007. Tsunami propagation modelling—a sensitivity study. *Natural*
928 *Hazards and Earth System Sciences*, 7(6), 741-754. [https://doi.org/10.5194/nhess-7-741-](https://doi.org/10.5194/nhess-7-741-2007)
929 [2007](https://doi.org/10.5194/nhess-7-741-2007)

930 Delpy, M., Lastiri, X., Abadie, S., Roeber, V., Maron, P., Liria, P., & Mader, J. (2021).
931 Characterization of the wave resource variability in the French Basque coastal area based
932 on a high-resolution hindcast. *Renewable Energy*, 178, 79-95.
933 <https://doi.org/10.1016/j.renene.2021.05.167>

934 DeMets, C., Jansma, P. E., Mattioli, G. S., Dixon, T. H., Farina, F., Bilham, R., Calais, E. & Mann, P.,
935 2000. GPS geodetic constraints on Caribbean-North America plate motion. *Geophysical*
936 *Research Letters*, 27(3), 437-440. <https://doi.org/10.1029/1999GL005436>

937 De Min, L., 2014. Sismo-stratigraphie multi-échelles d'un bassin d'avant-arc: le bassin de Marie-
938 Galante, Petites Antilles (Doctoral dissertation, Antilles-Guyane).

939 De Min, L., Lebrun, J. F., Cornée, J. J., Münch, P., Léticée, J. L., Quillévéré, F., Melinte-Dobrinescu, M.,
940 Randrianasolo, A., Marcaillou, B. & Zami, F., 2015. Tectonic and sedimentary architecture of
941 the Karukéra spur: A record of the Lesser Antilles fore-arc deformations since the Neogene.
942 *Marine Geology*, 363, 15-37. <https://doi.org/10.1016/j.margeo.2015.02.007>

943 Deplus C., 1998, AGUADOMAR cruise, RV L'Atalante, <https://doi.org/10.17600/98010120>

944 Dix, C.H., 1955. Seismic Velocities from Surface Measurements, *Geophysics* 20, no. 1, 68-86.
945 <https://doi.org/10.1190/1.1438126>

946 Deplus, C., Le Friant, A., Boudon, G., Komorowski, J.C., Villemant, B., Harford, C., Ségoufin, J. and Cheminée,
947 J.L., 2001. Submarine evidence for large-scale debris avalanches in the Lesser Antilles Arc. *Earth
948 and Planetary Science Letters*, 192(2), pp.145-157.

949 do Carmo, J. S. A. (2022). Dominant processes that amplify the swell towards the coast: the
950 Nazaré Canyon and the giant waves. *Research, Society and Development*, 11(11),
951 e578111133804-e578111133804. <https://doi.org/10.33448/rsd-v11i11.33804>

952 Escartín, J., Leclerc, F., Olive, J. A., Mevel, C., Cannat, M., Petersen, S., Augustin, N., Feuillet, N.,
953 Deplus, C., Bezos, A., Bonnemains, D., Chavagnac, V., Choi, Y., Godard, M., Haaga, K., Hamelin,
954 C., Ildefonse, B., Jamieson, J.W., John, B.E., Leleu, T., MacLead, C.J., Massot-Campos, M.,
955 Nomikou, P., Paquet, M., Tominaga, M., Triebe, L., Campos, R., Gracias, N., Garcia, R.,
956 Andreani, M. & Vilaseca, G. (2016). First direct observation of coseismic slip and seafloor
957 rupture along a submarine normal fault and implications for fault slip history. *Earth and
958 Planetary Science Letters*, 450, 96-107. <https://doi.org/10.1016/j.epsl.2016.06.024>

959 Escartin, J., Leclerc, F., Nathalie, F., Le Friant, A., Billant, J., Olive, J. A. L., Henri, M., Andreani, M.,
960 Arnaubec, A., Dano, A., Delorme, A., Deplus, C., Fournasson, M.L., Gini, C., Gracias, N.,
961 Hamelin, C., Istenic, K., Komorowski, J.C., Marchand C., Mevel, C., Onstad, S., Quidelleur, X. &
962 Garcia, R. (2018, December). Mapping the M_w 6.3 2004 Les Saintes earthquake seafloor
963 rupture with deep-sea vehicles: Length, displacement, nature, and links between coseismic
964 deformation and erosion/sedimentation. In *AGU Fall Meeting Abstracts* (Vol. 2018, pp.
965 EP51D-1851).

Feuillet, N., 2000. Sismotectonique des Petites Antilles: Liaison entre activité sismique
et volcanique (Doctoral dissertation, Paris 7).

966 Feuillet, N., Manighetti, I., & Tapponnier, P., 2001. Extension active perpendiculaire à la
967 subduction dans l'arc des Petites Antilles (Guadeloupe, Antilles françaises). *Comptes*

968 Rendus de l'Académie des Sciences-Series IIA-Earth and Planetary Science, 333(9), 583-
969 590.

970 Feuillet, N., Manighetti, I., Tapponnier, P., & Jacques, E., 2002. Arc parallel extension and
971 localization of volcanic complexes in Guadeloupe, Lesser Antilles. *Journal of Geophysical*
972 *Research: Solid Earth*, 107(B12), ETG-3. <https://doi.org/10.1029/2001JB000308>

973 Feuillet, N., Tapponnier, P., Manighetti, I., Villemant, B., & King, G. C. P., 2004. Differential uplift
974 and tilt of Pleistocene reef platforms and Quaternary slip rate on the Morne-Piton normal
975 fault (Guadeloupe, French West Indies). *Journal of Geophysical Research: Solid Earth*,
976 109(B2). <https://doi.org/10.1029/2003JB002496>

977 Feuillet, N., Leclerc, F., Tapponnier, P., Beauducel, F., Boudon, G., Le Friant, A., Deplus, C., Lebrun,
978 J.F., Nercessian, A., Saurel, J.M. & Clément, V., 2010. Active faulting induced by slip
979 partitioning in Montserrat and link with volcanic activity: New insights from the 2009
980 GWADASEIS marine cruise data. *Geophysical Research Letters*, 37(19).
981 <https://doi.org/10.1029/2010GL042556>

982 Feuillet, N., Beauducel, F., & Tapponnier, P., 2011. Tectonic context of moderate to large historical
983 earthquakes in the Lesser Antilles and mechanical coupling with volcanoes. *Journal of*
984 *Geophysical Research: Solid Earth*, 116(B10). <https://doi.org/10.1029/2011JB008443>

985 Fujita, M., Ishikawa, T., Mochizuki, M., Sato, M., Toyama, S. I., Katayama, M., Kawai, K., Mastumoto,
986 Y., Yabuki, T., Asada, A. & Colombo, O. L., 2006. GPS/Acoustic seafloor geodetic observation:
987 method of data analysis and its application. *Earth, planets and space*, 58(3), 265-275.
988 <https://doi.org/10.1186/BF03351923>

989 GEBCO Compilation Group, 2021. GEBCO 2021 Grid (doi:10.5285/c6612cbe-50b3-0cff-e053-
990 6c86abc09f8f)

991 Geli, L., Çağatay, N., Gasperini, L., Favali, P., Henry, P., & Çifçi, G., 2011. ESONET WP4-
992 Demonstration Missions. MARMARA-DM final report.
993 <https://archimer.ifremer.fr/doc/00032/14324/>

994 Goldfinger, C., Nelson, C. H., Morey, A. E., Johnson, J. E., Patton, J. R., Karabanov, E. B., Gutierrez-
995 Pastor, J., Eriksson, A.T., Gracia, E., Dunhill, G., Enkin, R.J., Dallimore, A. & Vallier, T., 2012.
996 Turbidite event history—Methods and implications for Holocene paleoseismicity of the
997 Cascadia subduction zone(No. 1661-F). US Geological Survey.
998 <https://doi.org/10.3133/pp1661F>

- 999 Gonzalez, OL, Clouard, V., & Zahradnik, J., 2017. Moment tensor solutions along the central Lesser
1000 Antilles using regional broadband stations. *Tectonophysics*, 717, 214-225.
1001 <https://doi.org/10.1016/j.tecto.2017.06.024>
- 1002 Gusman, A.R., Supendi, P., Nugraha, A.D., Power, W., Latief, H., Sunendar, H., Widiyantoro, S.,
1003 Daryono, Wiyono, S.H., Hakim, A., Muhari, A., Wang, X., Burbidge, D., Palgunadi, K., Hamling,
1004 I., Daryono, M.R., 2019. Source model for the tsunami inside Palu Bay following the 2018
1005 Palu earthquake, Indonesia. *Geophysical Research Letters*, 46, 8721-8730,
1006 <https://doi.org/10.1029/2019GL082717>.
- 1007 Gusman, A.R., Roger, J., Power, W., Fry, B., Kaneko, Y., 2022. The 2021 Loyalty Islands earthquake
1008 (M_w 7.7): Tsunami waveform inversion and implications for tsunami forecasting for New
1009 Zealand. *Earth and Space Science*, e2022EA002346,
1010 <https://doi.org/10.1029/2022EA002346>.
- 1011 Gutscher, M. A., Royer, J. Y., Graindorge, D., Murphy, S., Klingelhoefer, F., Aiken, C., Cattaneo, A.,
1012 Barreca, G., Quetel, L., Riccobene, G., Petersen, F., Urlaub, M., Krastel, S., Gross, F., Kopp, H.,
1013 Margheriti, L. Beranzoli, L., 2019. Fiber optic monitoring of active faults at the seafloor: I
1014 the FOCUS project. *Photoniques*, 32-37. <https://doi.org/10.1051/photon/2019S432>
- 1015 Hirata, K., Aoyagi, M., Mikada, H., Kawaguchi, K., Kaiho, Y., Iwase, R., Morita, S., Fujisawa, I.,
1016 Sugioka, H., Mitsuzawa, K., Suyehiro, K. & Fujiwara, N., 2002. Real-time geophysical
1017 measurements on the deep seafloor using submarine cable in the southern Kurile
1018 subduction zone. *IEEE Journal of Oceanic Engineering*, 27(2), 170-181.
1019 <https://doi.org/10.1109/JOE.2002.1002471>
- 1020 IOC-UNESCO (2020). Experts Meeting on Sources of Tsunamis in the Lesser Antilles Fort-de-
1021 France, Martinique (France) 18–20 March 2019. Workshop Reports, (291), 55p. Open
1022 Access version : <https://archimer.ifremer.fr/doc/00665/77736/>
- 1023 Kido, M., Fujimoto, H., Miura, S., Osada, Y., Tsuka, K., & Tabei, T., 2006. Seafloor displacement at
1024 Kumano-nada caused by the 2004 off Kii Peninsula earthquakes, detected through repeated
1025 GPS/Acoustic surveys. *Earth, planets and space*, 58(7), 911-915.
1026 <https://doi.org/10.1186/BF03351996>
- 1027 Kopp, H., Weinzierl, W., Becel, A., Charvis, P., Evain, M., Flueh, E. R., Gailler, A., Galve, A., Hirn, A.,
1028 Kandilarov, D., Klaeschen, D., Laigle, M., Papenberg, C., Planert, L. & Roux, E., 2011. Deep
1029 structure of the central Lesser Antilles Island Arc: relevance for the formation of
1030 continental crust. *Earth and Planetary Science Letters*, 304(1-2), 121-134.
1031 <https://doi.org/10.1016/j.epsl.2011.01.024>

1032 Laigle M., Lebrun J.-F., Hirn A. (2007) SISMANTILLES 2 cruise, RV L'Atalante,
1033 <https://doi.org/10.17600/7010020>

1034 Lander, J. F., & Whiteside, L. S., 1997. Caribbean tsunamis: an initial history. In Caribbean
1035 Tsunami Workshop, June (pp. 11-13).

1036 Lander, J. F., Whiteside, L. S., & Lockridge, P. A., 2003. Two decades of global tsunamis. *Science of*
1037 *Tsunami Hazards*, 21(1), 3.

1038 Lardeaux, J. M., Münch, P., Corsini, M., Cornée, J. J., Verati, C., Lebrun, J. F., Guillevere, F., Melinte-
1039 Dobrinescu, M., Leticee, J.L., Fietzke, J., Mazabraud, Y., Cordrey, F. & Randrianasolo, A., 2013.
1040 La Désirade island (Guadeloupe, French West Indies): a key target for deciphering the role
1041 of reactivated tectonic structures in Lesser Antilles arc building. *Bulletin de la Société*
1042 *géologique de France*, 184(1-2), 21-34. <https://doi.org/10.2113/gssgfbull.184.1-2.21>

1043 Laurencin, M., Graindorge, D., Klingelhofer, F., Marcaillou, B., & Evain, M., 2018. Influence of
1044 increasing convergence obliquity and shallow slab geometry onto tectonic deformation and
1045 seismogenic behavior along the Northern Lesser Antilles zone. *Earth and Planetary Science*
1046 *Letters*, 492, 59-72. <https://doi.org/10.1029/2019GL083490>

1047 Lebrun, J.-F., Cornée, J.-J., Münch, P., Guennoc, P., Thinon, I., Begot, J., Mazabraud, Y., Fournier, F.,
1048 Feuillet, N., Randrianasolo, A., 2008. La Mission KaShallow 1 - N/O Antéa - 26 avril - 05 Mai
1049 - Sismique réflexion haute résolution dans le bassin de Marie-Galante - Avant-arc des
1050 Petites Antilles. Rapport de l'Université des Antilles et de la Guyane.

1051 Leclerc, F., Feuillet, N., & Deplus, C., 2016. Interactions between active faulting, volcanism, and
1052 sedimentary processes at an island arc: Insights from Les Saintes channel, Lesser Antilles
1053 arc. *Geochemistry, Geophysics, Geosystems*, 17(7), 2781-2802.
1054 <https://doi.org/10.1002/2016GC006337>

1055 Le Friant, A., Heinrich, P., & Boudon, G., 2008. Field survey and numerical simulation of the 21
1056 November 2004 tsunami at Les Saintes (Lesser Antilles). *Geophysical Research Letters*,
1057 35(12). <https://doi.org/10.1029/2008GL034051>

1058 Le Friant, A., Boudon, G., Arnulf, A., & Robertson, R. E. (2009). Debris avalanche deposits offshore St.
1059 Vincent (West Indies): impact of flank-collapse events on the morphological evolution of the island.
1060 *Journal of Volcanology and Geothermal Research*, 179(1-2), 1-10.

1061 Le Friant, A., Lebas, E., Brunet, M., Lafuerza, S., Hornbach, M., Coussens, M., Watt, S., Cassidy, M., Talling,
1062 P.J. and IODP 340 Expedition Science Party (2019). Submarine landslides around volcanic islands:
1063 A review of what can be learned from the Lesser Antilles Arc. *Submarine Landslides: Subaqueous*
1064 *Mass Transport Deposits from Outcrops to Seismic Profiles*, pp.277-297.

1065 Legendre, L., Philippon, M., Münch, P., Leticee, J. L., Noury, M., Maincent, G., Cornee, J.J., Caravati,
1066 A., Lebrun, J.F. & Mazabraud, Y., 2018. Trench bending initiation: Upper plate strain pattern
1067 and volcanism. insights from the Lesser Antilles arc, St. Barthelemy island, French West
1068 Indies. *Tectonics*, 37(9), 2777-2797.

1069 Lehu, R., Lallemand, S., Ratzov, G., Babonneau, N., Hsu, S. K., Lin, A. T., & Dezileau, L., 2016. An
1070 attempt to reconstruct 2700 years of seismicity using deep-sea turbidites offshore eastern
1071 Taiwan. *Tectonophysics*, 692, 309-324. <https://doi.org/10.1016/j.tecto.2016.04.030>

1072 Leticee, J. L., Cornee, J. J., Münch, P., Fietzke, J., Philippon, M., Lebrun, J. F., De Min, L., &
1073 Randrianasolo, A., 2019. Decreasing uplift rates and Pleistocene marine terraces settlement
1074 in the central lesser Antilles fore-arc (La Désirade Island, 16° N). *Quaternary International*,
1075 508, 43-59. <https://doi.org/10.1016/j.quaint.2018.10.030>

1076 Leslie, S. C., & Mann, P. (2016). Giant submarine landslides on the Colombian margin and tsunami risk in
1077 the Caribbean Sea. *Earth and Planetary Science Letters*, 449, 382-394.

1078 Lewis, K. B. (1980). Quaternary sedimentation on the Hikurangi oblique-subduction and
1079 transform margin, New Zealand. *Sedimentation in oblique-slip mobile zones*, 171-189.
1080 <https://doi.org/10.1002/9781444303735.ch10>

1081 Liu, P.L.F., Woo, S.B., Cho, Y.S., 1998. Computer programs for tsunami propagation and
1082 inundation. Ithaca (NY): Cornell University. Technical Report.

1083 Mallet, R., 1853. Catalogue of Recorded Earthquakes from 1606 B.C. to A.D. 1850, Part I, 1606
1084 B.C. to 1755 A.D. Report of the 22nd Meeting of the British Association for the Advancement
1085 of Science, held in Belfast, Sept. 1852, John Murray, London, 177 pp.

1086 Mallet R. (1854). Catalogue of Recorded Earthquakes from 1606 B.C. to A.D. 1850, Part II, 1755
1087 A.D. to 1784 A.D., Report of the 23rd meeting of the British Association for the
1088 Advancement of Science, held in Hull, Sept. 1853, John Murray, London, 118-212.

1089 Mallet R. (1855). Catalogue of Recorded Earthquakes from 1606 B.C. to A.D. 1850, Part III, 1784
1090 A.D. to 1842 A.D., Report of the 24th Meeting of the British Association for the Advancement
1091 of Science, John Murray, London, 326 pp.

1092 Martins, I., Vitorino, J., & Almeida, S. (2010, May). The Nazare Canyon observatory (W Portugal)
1093 real-time monitoring of a large submarine canyon. In *OCEANS'10 IEEE SYDNEY* (pp. 1-7).
1094 IEEE.

1095 Martínez-Loriente, S., Sallarès, V., & Gràcia, E., 2021. The Horseshoe Abyssal plain Thrust could
1096 be the source of the 1755 Lisbon earthquake and tsunami. *Communications earth &*
1097 *environment*, 2(1), 145. <https://doi.org/10.1038/s43247-021-00216-5>

1098 Massin, F., Clouard, V., Vorobieva, I., Beauducel, F., Saurel, J. M., Satriano, C., Bouin, M. P., & Bertil,
1099 D. (2021). Automatic picking and probabilistic location for earthquake assessment in the
1100 lesser antilles subduction zone (1972-2012). In *Comptes Rendus - Geoscience* (Vol. 353,
1101 Issue S1). Academie des sciences. <https://doi.org/10.5802/crgeos.81>.
1102 <https://doi.org/10.5802/crgeos.81>

1103 McCalpin, J.P. 1996. (Ed.), *Paleoseismology*, Academic Press, London, p. 583

1104 Münch, P., Lebrun, J. F., Cornée, J. J., Thinon, I., Guennoc, P., Marcaillou, B. J., Begot, J., Bertrand, G.,
1105 Bes De Berc, S., Biscarrat, K., Claud, C., De Min, L., Fournier, F., Gailler, L., Grandorge, D.,
1106 Leticee, J.L., Marie, L., Mazabraud, Y., Melinte-Dobrinescu, M., Moissette, P., Quilevere, F.,
1107 Verati, C. & Randrianasolo, A., 2013. Pliocene to Pleistocene carbonate systems of the
1108 Guadeloupe archipelago, French Lesser Antilles: a land and sea study (the KaShallow
1109 project). *Bulletin de la Société géologique de France*, 184(1-2), 99-110.
1110 <https://doi.org/10.2113/gssgfbull.184.1-2.99>

1111 Münch, P., Cornee, J. J., Lebrun, J. F., Quillevere, F., Verati, C., Melinte-Dobrinescu, M., Demory, B.,
1112 Smith, F., Jourdan, J.M., Lardeaux, J.M., De Min, L., Leticee, J.L. & Randrianasolo, A., 2014.
1113 Pliocene to Pleistocene vertical movements in the forearc of the Lesser Antilles subduction:
1114 insights from chronostratigraphy of shallow-water carbonate platforms (Guadeloupe
1115 archipelago). *Journal of the Geological Society*, 171(3), 329-341.
1116 <https://doi.org/10.1144/jgs2013-005>

1117 NASA Shuttle Radar Topography Mission (SRTM)(2013). Shuttle Radar Topography Mission
1118 (SRTM) Global. Distributed by OpenTopography. <https://doi.org/10.5069/G9445JDF>.
1119 Accessed: 2022-12-07.

1120 Nikolcina, I., Zahibo, N., & Pelinovsky, E., 2010. Tsunami in Guadeloupe (Caribbean Sea). *The*
1121 *Open Oceanography Journal*, 4(1). <https://doi.org/10.2174/1874252101004010044>

1122 Okada, Y., 1985. Surface deformation due to shear and tensile faults in a half-space. *Bulletin of*
1123 *the seismological society of America*, 75(4), 1135-1154.
1124 <https://doi.org/10.1785/BSSA0750041135>

1125 O'loughlin, K. F., & Lander, J. F., 2003. *Caribbean tsunamis: a 500-year history from 1498-1998*
1126 (Vol. 20). Springer Science & Business Media.

1127 Padron, C., Klingelhofer, F., Marcaillou, B., Lebrun, J. F., Lallemand, S., Garrocq, C., Laigle, M.,
1128 Roest, W.R., Beslier, M.O., Schenini, L., Graindorge, D., Gay, A., Audemard, F., Munch, P. &
1129 GARANTI Cruise Team., 2021. Deep structure of the Grenada Basin from wide-angle

1130 seismic, bathymetric and gravity data. *Journal of Geophysical Research: Solid Earth*, 126(2),
1131 e2020JB020472. <https://doi.org/10.1029/2020JB020472>

1132 Paris, R., Sabatier, P., Biguenet, M., Bougouin, A., André, G., Roger, J., 2021. A tsunami deposit at
1133 Anse Meunier, Martinique Island: evidence of the 1755 CE Lisbon tsunami and implication
1134 for hazard assessment. *Marine Geology*, 439, 106561,
1135 <https://doi.org/10.1016/j.margeo.2021.106561>.

1136 Petersen, F., Kopp, H., Lange, D., Hannemann, K., & Urlaub, M., 2019. Measuring tectonic seafloor
1137 deformation and strain-build up with acoustic direct-path ranging. *Journal of Geodynamics*,
1138 124, 14-24. <https://doi.org/10.1016/j.jog.2019.01.002>

1139 Philippon, M., & Corti, G., 2016. Obliquity along plate boundaries. *Tectonophysics*, 693, 171-182.
1140 <https://doi.org/10.1016/j.tecto.2016.05.033>

1141 Prasetya, G., Beavan, J., Wang, X., Reyners, M., Power, W., Wilson, K., Lukovic, B., 2011. Evaluation
1142 of the 15 July 2009 Fjorland, New Zealand tsunami in the source region. *Pure and Applied*
1143 *Geophysics*, 168, 1973-1987, <https://doi.org/10.1007/s00024-011-0282-6>.

1144 Roger, J., Allgeyer, S., Hébert, H., Baptista, M. A., Loevenbruck, A., & Schindelé, F., 2010. The 1755
1145 Lisbon tsunami in Guadeloupe Archipelago: source sensitivity and investigation of
1146 resonance effects. *The Open Oceanography Journal*, 4(1).
1147 <https://doi.org/10.2174/1874252101004010058>

1148 Roger, J., Baptista, M. A., Sahal, A., Accary, F., Allgeyer, S., & Hébert, H., 2011. The transoceanic
1149 1755 Lisbon tsunami in Martinique. *Pure and Applied Geophysics*, 168(6), 1015-1031.
1150 <https://doi.org/10.1007/s00024-010-0216-8>

1151 Roger, J., Dudon, B., & Zahibo, N., 2013. Tsunami hazard assessment of Guadeloupe Island (FWI)
1152 related to a megathrust rupture on the Lesser Antilles subduction interface. *Natural*
1153 *Hazards and Earth System Sciences*, 13(5), 1169-1183. [https://doi.org/10.5194/nhess-13-](https://doi.org/10.5194/nhess-13-1169-2013)
1154 1169-2013

1155 Roger, J., Pelletier, B., & Aucan, J. (2019). Update of the tsunami catalogue of New Caledonia using
1156 a decision table based on seismic data and marigraphic records. *Natural Hazards and Earth*
1157 *System Sciences*, 19(7), 1471-1483. <https://doi.org/10.5194/nhess-19-1471-2019>

1158 Roger, J., Pelletier, B., Gusman, A., Power, W., Wang, X., Burbidge, D., & Duphil, M., 2023. Potential
1159 tsunami hazard of the southern Vanuatu Subduction Zone: tectonics, case study of the
1160 Matthew Island tsunami of 10 February 2021 and implication in regional hazard
1161 assessment. *Natural Hazards and Earth System Sciences*, 23(2), 393-414,
1162 <https://doi.org/10.5194/nhess-23-393-2023>.

- 1163 Roger, J.H., Bull, S., Watson, S.J., Mueller, C., Hillman, J.I., Wolter, A., Lamarche, G., Power, W., Lane,
 1164 E., Woelz, S. and Davidson, S. (2024). A review of approaches for submarine landslide-
 1165 tsunami hazard identification and assessment. *Marine and Petroleum Geology*,
 1166 162(106729), <https://doi.org/10.1016/j.marpetgeo.2024.106729>.
- 1167 Ruiz, M., Galve, A., Monfret, T., Sapin, M., Charvis, P., Laigle, M., Evain, M., Hirn, A., Flueh, E., Gallart,
 1168 K., Diaz, J., Lebrun, J.F. & Lebrun, J. F., 2013. Seismic activity offshore Martinique and
 1169 Dominica islands (Central Lesser Antilles subduction zone) from temporary onshore and
 1170 offshore seismic networks. *Tectonophysics*, 603, 68-78.
 1171 <https://doi.org/10.1016/j.tecto.2011.08.006>
- 1172 Salichon, J., Lemoine, A., Aochi, H., 2009. Validation of teleseismic inversion of the 2004 M_w 6.3
 1173 Les Saintes, Lesser Antilles, earthquake by 3D finite-difference forward modelling. *Bull.*
 1174 *Seismol. Soc. Am.* 99, 3390–3401. <https://doi.org/10.1785/0120080315>
- 1175 Satake, K., & Tanioka, Y., 1999. Sources of tsunami and tsunamigenic earthquakes in subduction
 1176 zones. *Pure and Applied Geophysics*, 154(3), 467-483.
 1177 <https://doi.org/10.1785/0120120306>
- 1178 Seibert, C., Feuillet, N., Ratzov, G., Beck, C., & Cattaneo, A., 2020. Seafloor morphology and
 1179 sediment transfer in the mixed carbonate-siliciclastic environment of the Lesser Antilles
 1180 forearc along Barbuda to St. Lucia. *Marine Geology*, 428, 106242.
 1181 <https://doi.org/10.1016/j.margeo.2020.106242>
- 1182 [Smith, M. S., & Shepherd, J. B. \(1996\). Tsunami waves generated by volcanic landslides: an assessment of
 1183 the hazard associated with Kick'em Jenny. Geological Society, London, Special Publications, 110\(1\),
 1184 115-123.](#)
- 1185 Symithe, S. J., Calais, E., Haase, J. S., Freed, A. M., & Douilly, R., 2013. Coseismic slip distribution of
 1186 the 2010 M 7.0 Haiti earthquake and resulting stress changes on regional faults. *Bulletin of*
 1187 *the Seismological Society of America*, 103(4), 2326-2343.
 1188 <https://doi.org/10.1785/0120120306>
- 1189 ten Brink, U., Danforth, W., Polloni, C., Andrews, B., Llanes, P., Smith, S., Parker, E., and Uozumi, T.
 1190 2004. New seafloor map of the Puerto Rico trench helps assess earthquake and tsunami
 1191 hazards. *Eos, Transactions American Geophysical Union* 85: 349–360.
 1192 [doi:10.1029/2004EO370001](https://doi.org/10.1029/2004EO370001).
- 1193 Terrier, M., Combes P. avec la collaboration de D. Carbon, B. Grellet, O. Sedan (2002) - FAILLES
 1194 ACTIVES ET EVALUATION DE L’ALEA SISMIQUE : Prise en compte des failles actives dans
 1195 l’aménagement du territoire aux Antilles (Martinique et Guadeloupe). Partie 1 :

1196 Identification des systèmes de failles actives dans l'archipel de la Guadeloupe et l'île de la
1197 Martinique. Rapport BRGM/RP-51258-FR. 118 pages. 30 figures. 8 tableaux. 4 annexes
1198 Teeuw, R., Rust, D., Solana, C., Dewdney, C., & Robertson, R. (2009). Large coastal landslides and tsunami
1199 hazard in the Caribbean. *Eos, Transactions American Geophysical Union*, 90(10), 81-82.

1200 Thingbaijam, K.K.S., Mai, P.M. and Goda, K., 2017. New Empirical Earthquake Source-Scaling
1201 Laws. *Bulletin of the Seismological Society of America*, 107(5), pp.2225-2246.
1202 <https://doi.org/10.1785/0120170017>

1203 Thinon, I, Bitri, A., 2003. GEOBERYX03 cruise, RV Beryx, [Catalogue des campagnes à la mer](http://flotteoceanographique.fr)
1204 [\[flotteoceanographique.fr\]](http://flotteoceanographique.fr) ;browsed on-line on Seadatanet webportal
1205 (SISM_BGM_F1352003000010, <https://cdi.seadatanet.org/>);

1206 Thinon I., Bitri A., Guennoc P. & Truffert C. (2004). – Levés sismique et magnétique du plateau
1207 occidental de l'île de Basse-Terre, Guadeloupe (Campagne Geoberyx03). Apports à la
1208 compréhension du contexte structural du champ géothermique de Bouillante. – BRGM/RP-
1209 53152-FR, 77.

1210 Thinon, I., Guennoc, P., Bitri, A., Truffert C., 2010, Study of the Bouillante Bay (West Basse-Terre
1211 Island shelf): contribution of geophysical surveys to the understanding of the structural
1212 context of Guadeloupe (French West Indies - Lesser Antilles). *Bull. Soc. Geol. Fr.*, 181, 51-
1213 65, <http://doi.org/10.2113/gssgfbull.181.1.51>

1214 TL/ICMMG (2023). Global Historical Tsunami Database. Institute of Computational Mathematics
1215 and Mathematical Geophysics SB RAS Tsunami Laboratory, Novosibirsk, Russia,
1216 <http://tsun.sccc.ru/gtdb/default.aspx> (last accessed on 1 February 2023).

1217 Tronin, A. A., 2009. Satellite remote sensing in seismology. A review. *Remote Sensing*, 2(1), 124-
1218 150. <https://doi.org/10.3390/rs2010124>

1219 van Rijnsingen, E. M., Calais, E., Jolivet, R., de Chabalière, J. B., Jara, J., Symithe, S., ... & Ryan, G. A.,
1220 2021. Inferring interseismic coupling along the lesser antilles arc: A Bayesian approach.
1221 *Journal of Geophysical Research: Solid Earth*, 126(2), e2020JB020677.
1222 <https://doi.org/10.1029/2020JB020677>

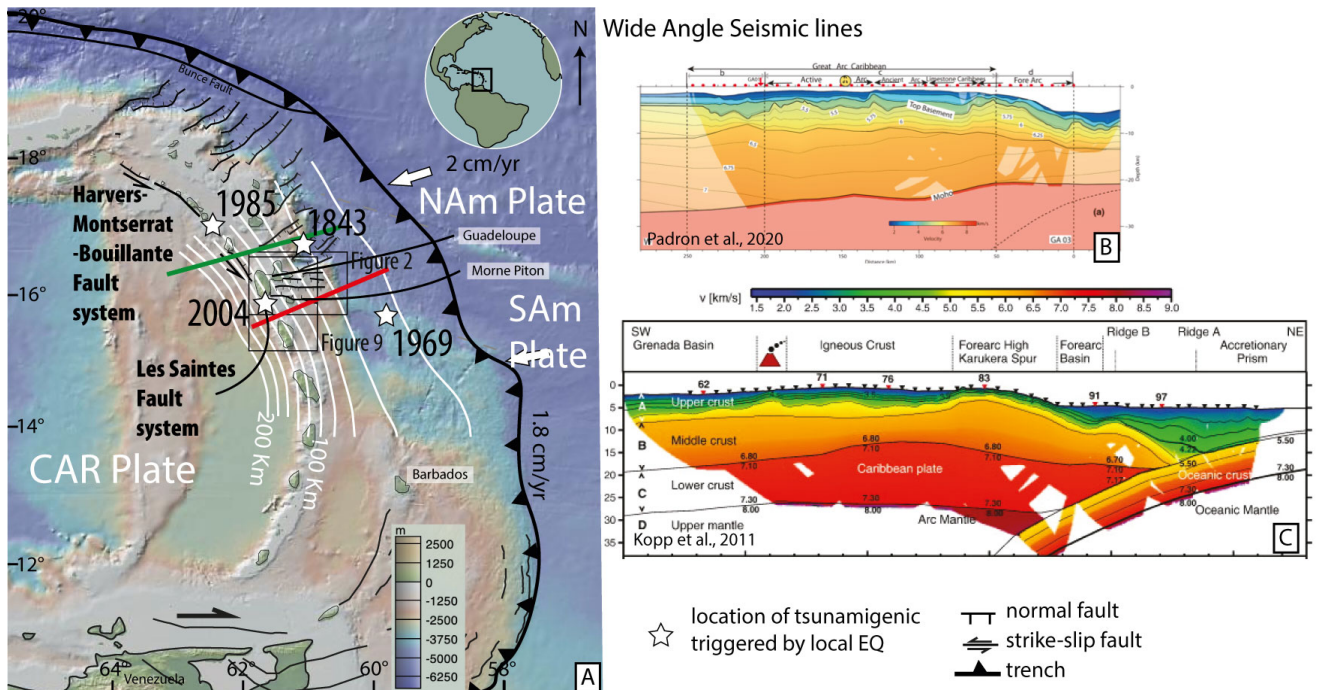
1223 Wallace, T. C., Helmberger, D. V., & Ebel, J. E., 1981. A broadband study of the 13 August 1978
1224 Santa Barbara earthquake. *Bulletin of the Seismological Society of America*, 71(6), 1701-
1225 1718. <https://doi.org/10.1785/BSSA0710061701>

1226 Wang, X., 2008. Numerical modelling of surface and internal waves over shallow and
1227 intermediate water [PhD thesis]. Ithaca (NY): Cornell University. 245 p.

- 1228 Wang, X., Power, W.L., 2011. COMCOT: a tsunami generation, propagation and run-up model.
1229 Lower Hutt (NZ): GNS Science. 121 p. (GNS Science report; 2011/43).
- 1230 Wang X, Lukovic B, Power WL, Mueller C., 2017. High-resolution inundation modelling with
1231 explicit buildings. Lower Hutt (NZ): GNS Science. 27 p. (GNS Science report 2017/13).
1232 <https://doi.org/10.21420/G2RW2N>.
- 1233 Wells, D. L., & Coppersmith, K. J., 1994. New empirical relationships among magnitude, rupture
1234 length, rupture width, rupture area, and surface displacement. Bulletin of the seismological
1235 Society of America, 84(4), 974-1002. <https://doi.org/10.1785/BSSA0840040974>
- 1236 Wessel, P., Luis, J.F., Uieda, L., Scharroo, R., Wobbe, F., Smith, W.H.F., Tian, D., 2019. The Generic
1237 Mapping Tools Version 6. Geochemistry, Geophysics, Geosystems, 20(11), 5556-5564,
1238 <https://doi.org/10.1029/2019GC008515>.
- 1239 Yamazaki, Y., Cheung, K. F., & Lay, T., 2013. Modeling of the 2011 Tohoku near-field tsunami from
1240 finite-fault inversion of seismic waves. Bulletin of the Seismological Society of America,
1241 103(2B), 1444-1455. <https://doi.org/10.1785/0120120103>
- 1242 Zahibo, N., Pelinovsky, E., Kurkin, A., & Kozelkov, A., 2003. Estimation of far-field tsunami
1243 potential for the Caribbean Coast based on numerical simulation. Science of Tsunami
1244 Hazards, 21(4), 202-222.
- 1245 Zahibo, N., Pelinovsky, E., Okal, E., Yalçiner, A., Kharif, C., Talipova, T., & Kozelkov, A., 2005. The
1246 earthquake and tsunami of November 21, 2004 at Les Saintes, Guadeloupe, Lesser Antilles.
1247 Science of Tsunami Hazards, 23(1), 25-39.
- 1248 Zhang, L., Baba, K., Liang, P., Shimizu, H., & Utada, H., 2014. The 2011 Tohoku Tsunami observed
1249 by an array of ocean bottom electromagnetometers. Geophysical Research Letters, 41(14),
1250 4937-4944. <https://doi.org/10.1002/2014GL060850>
- 1251

1252 FIGURES

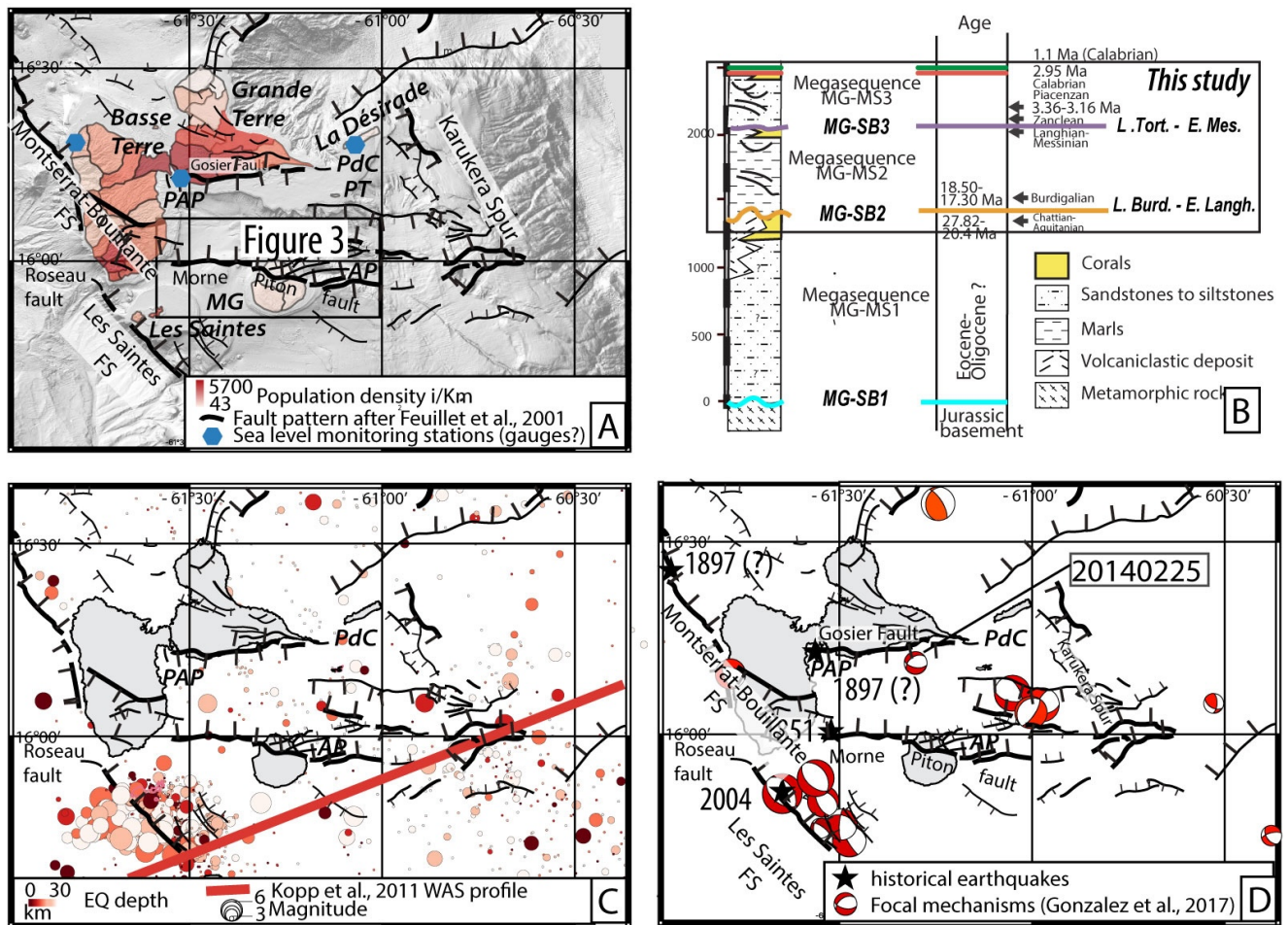
1253



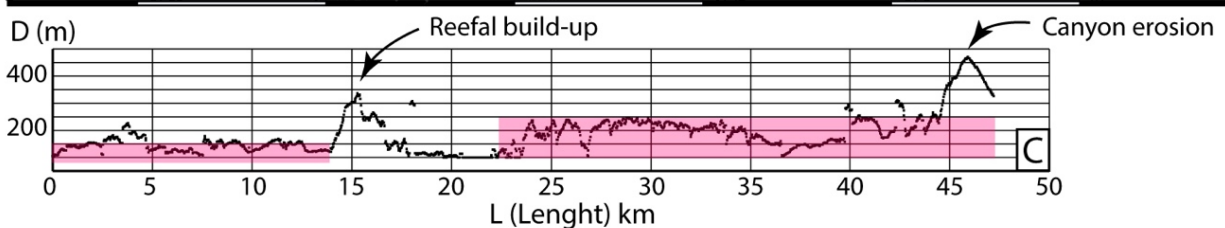
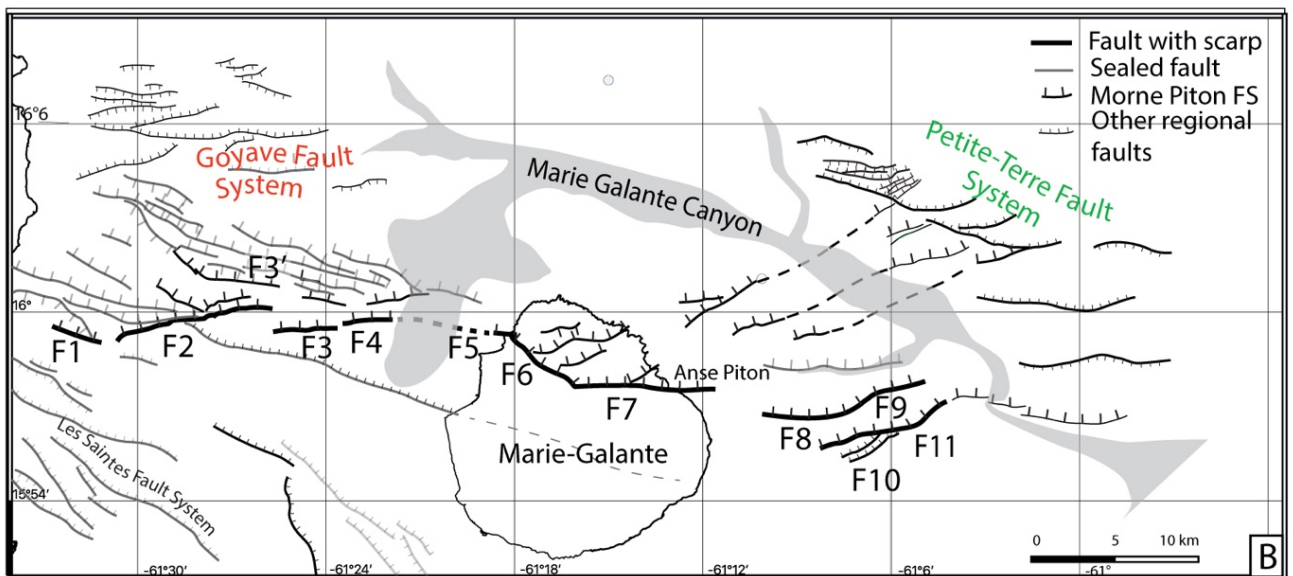
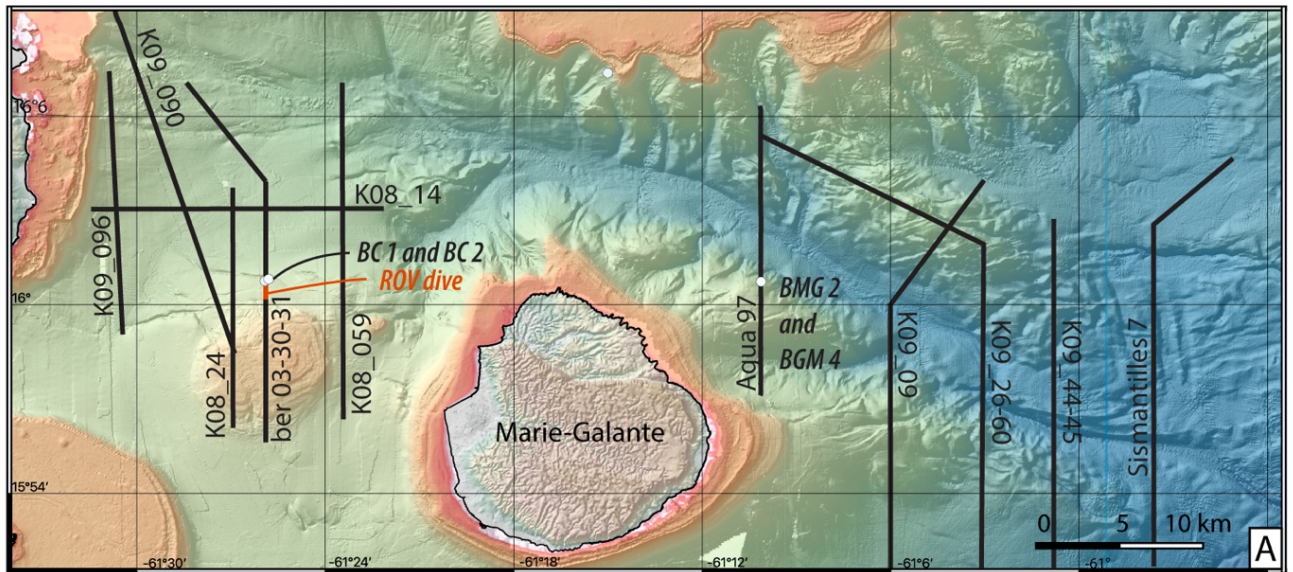
1254

1255 *Figure 1: A: Synthetic tectonic map of the Lesser Antilles forearc. Structures after Feuillet et al.*
1256 *(2002), De Min (2014), Laurencin et al. (2019), Legendre (2018), Boucard et al. (2021). Red and*
1257 *green thick lines indicate location of the Wide Angle Seismic lines from B. Kopp et al. (2011) and C.*
1258 *Padron et al. (2021) respectively. White Star: location of tsunamigenic earthquakes. Thick white*
1259 *contour lines: Slab depth isocontour from Bie et al. (2020).*

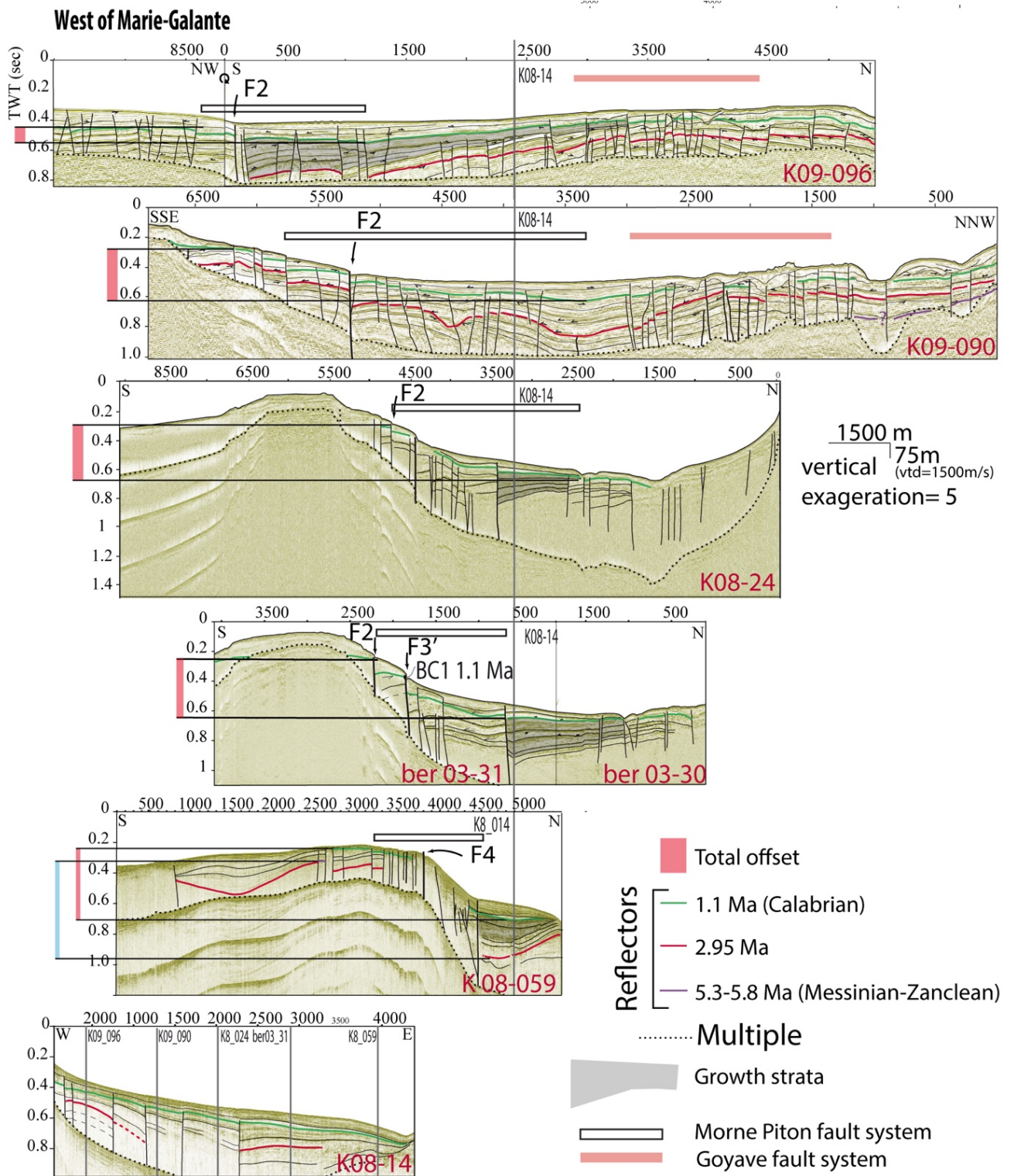
1260



1261
 1262 *Figure 2. The Marie-Galante Basin A) structural pattern after Feuillet et al. (2002) and De Min et*
 1263 *al. (2015) on the shaded-relief bathymetric map. blue hexagons : tide gauges*
 1264 *<http://refmar.shom.fr/fr/liste-maregraphes-data.shom.fr>. Red colors scale: Guadeloupe*
 1265 *population density per km2 after GEOFLA (<https://www.data.gouv.fr/fr/datasets/geofla-r/>). B)*
 1266 *Sismostratigraphic scheme of the Marie-Galante basin modified after Cornée et al., 2023. C) Colored*
 1267 *dots: Crustal seismicity (from IRIS seismic database 2023) for magnitude earthquakes (EQ)*
 1268 *$3 > M_w > 6.5$ and located from 0 to 30 km depth), red line locates the WAS line (Kopp et al., 2011). D)*
 1269 *Focal mechanisms solutions are indicated by red beachballs after Gonzalez et al. (2017). The*
 1270 *location of historical earthquakes is indicated by black stars (after: Feuillet et al., 2011b). AP, PdC,*
 1271 *PAP, PT stand for Anse Piton, Pointe des Chateaux, Pointe-à-Pitre and Petite Terre.*
 1272



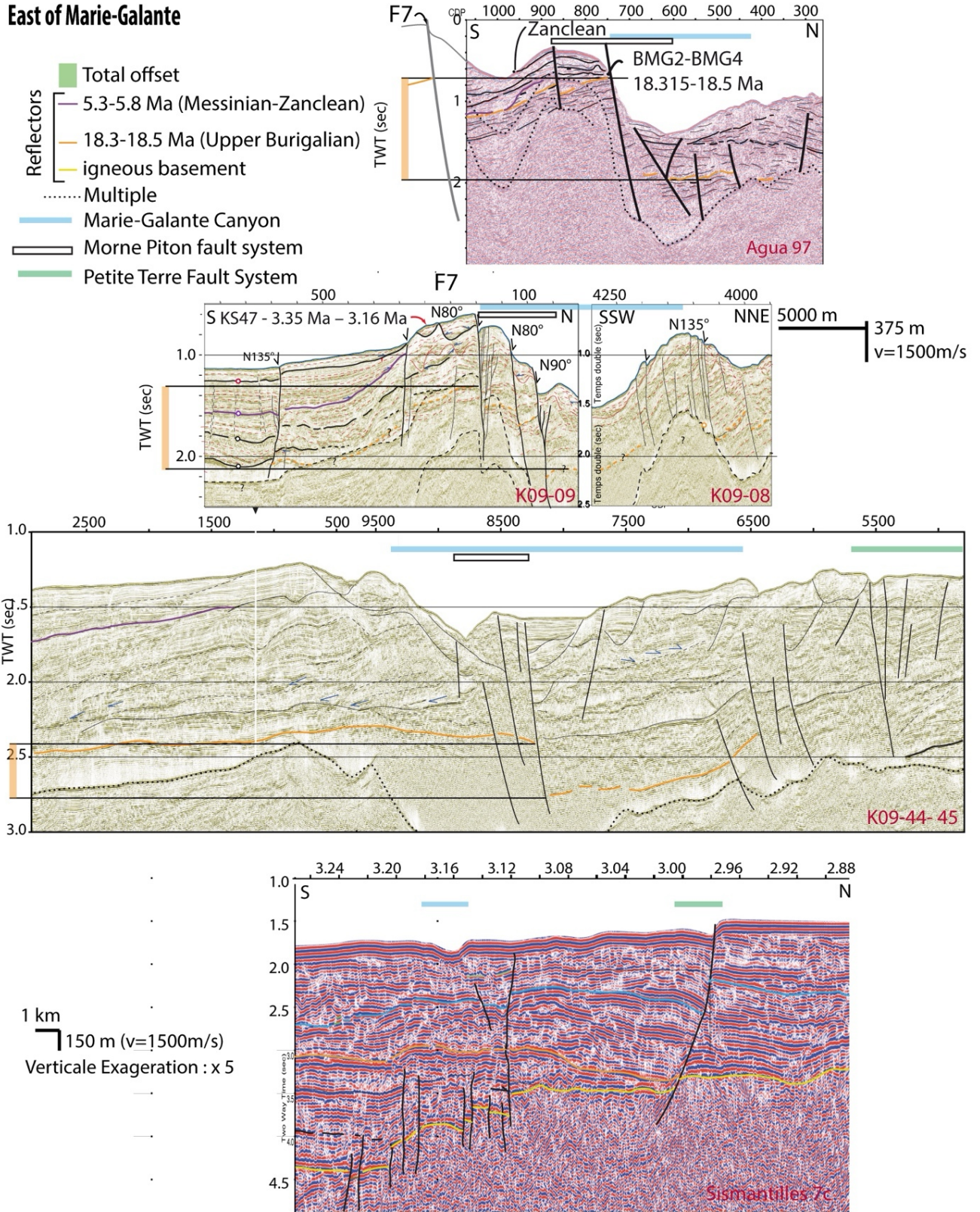
1273
 1274 Figure 3. A) High resolution (25m grid spacing) bathymetric map [UMO16] of the Marie-Galante Basin,
 1275 offshore Guadeloupe and location of the seismic profiles shown on figures 4 and 5, and location of
 1276 dredge samples used for the seismic units age calibration (Münch et al. 2013). B) Structural
 1277 interpretation of the E-W trending Morne Piton fault system. C) A proxy for cumulative strain given
 1278 by the graphic displaying the D (fault surface displacement) taken as the difference between the top
 1279 and the toe of the fault scarp versus L (fault length) along the whole system.



1280
 1281 *Figure 4: Seismic lines West of Marie-Galante (location on Figure 3) showing the correlation across*
 1282 *the Morne Piton fault system of the 1.29Ma unit reflector (Green) that correspond to the reflector*
 1283 *dredged at BC1 and BC2 location along the Ber03_30-31 seismic line. The 2.95Ma Unit Boundary*
 1284 *(Red) is correlated from seismic lines south of the Colombie Bank and Eastern Marie-Galante Basin*
 1285 *(line K09_90 and K09_26-62 location on figure 2). Notice that the basin sedimentary slope is in the*

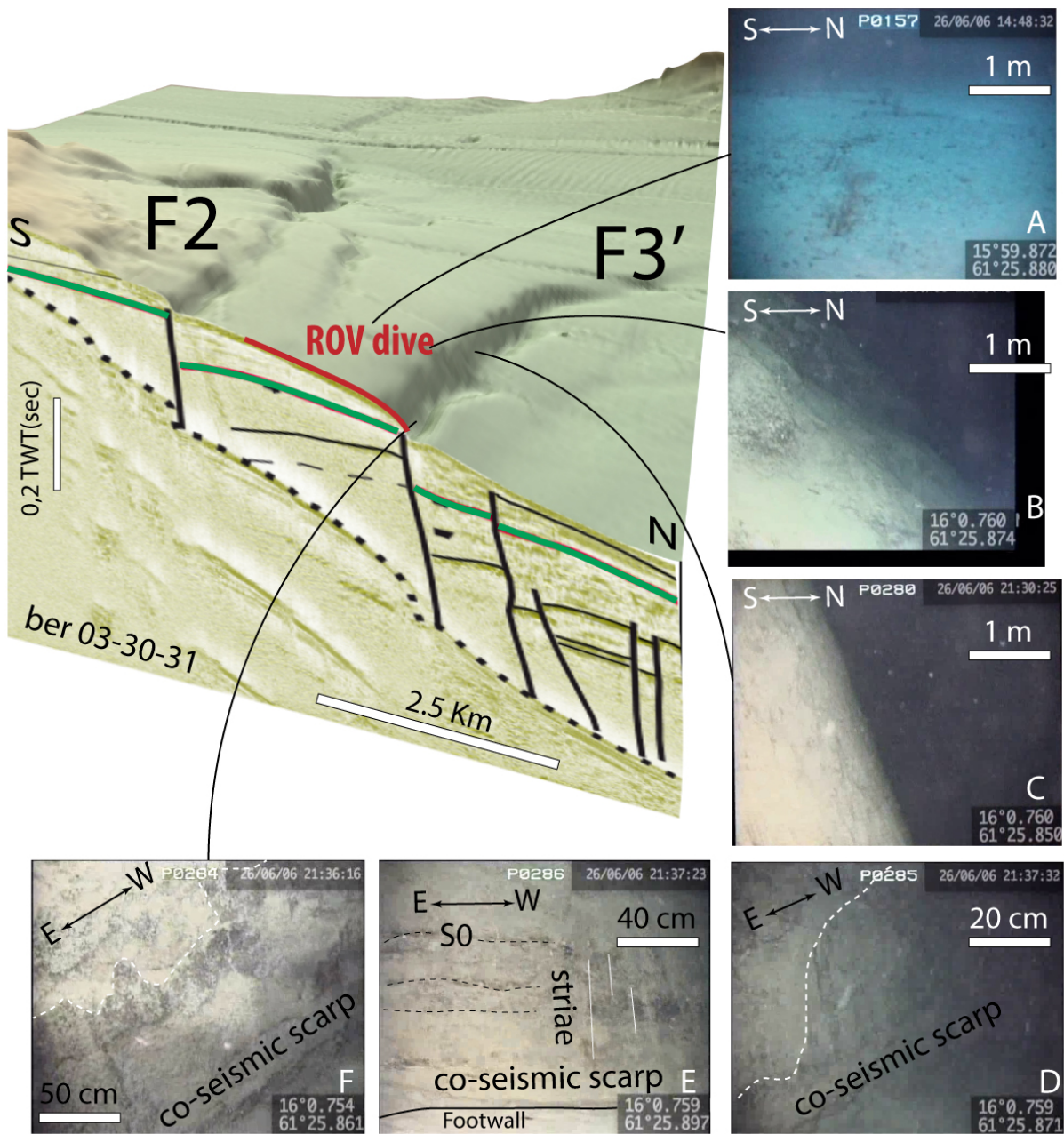
1286 E-W direction (parallel to line K08-14). Therefore, the initial topography of the reflectors in the N-
 1287 S direction, across the fault system, can be neglected when measuring the offset along the seismic
 1288 lines.

East of Marie-Galante



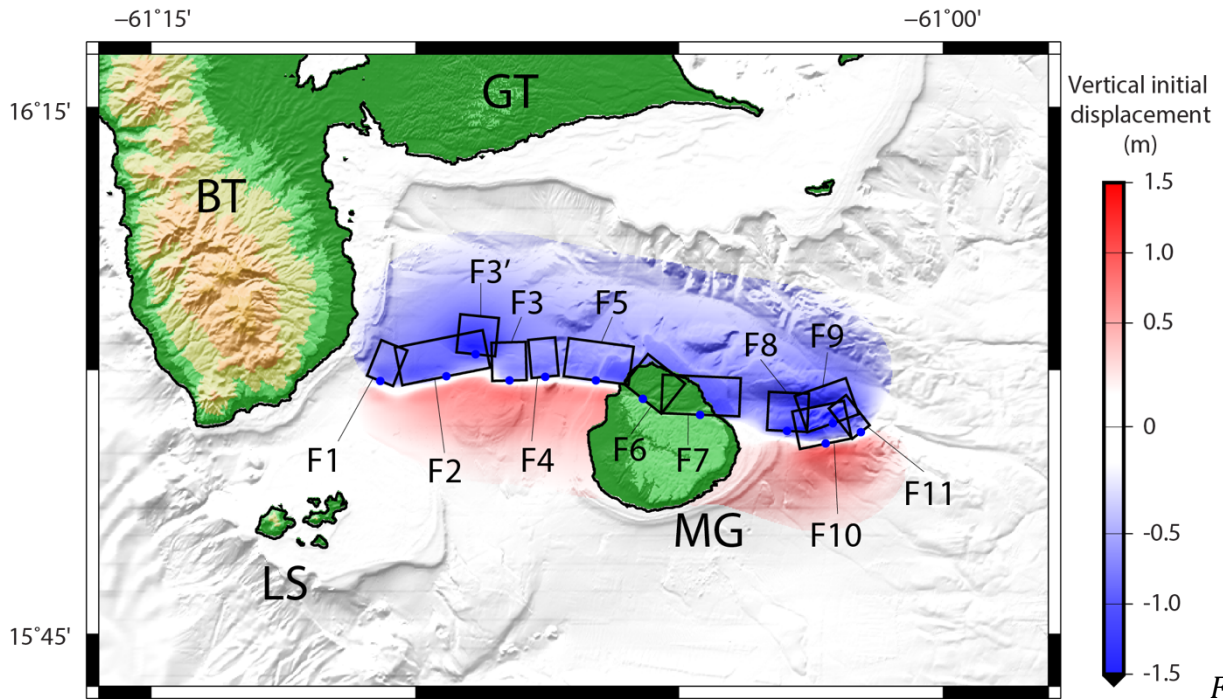
1289

1290 Figure 5: Seismic lines east of Marie-Galante illustrate the correlation across the Morne Piton fault
 1291 system of the 7 Ma (Tortonian/Messinian) MG-SB3 sequence boundary (Purple) and the 16 Ma,
 1292 (Burdigalian) MG-SB2 Sequence Boundary (Orange). Seismic line location on Figure 3).
 1293

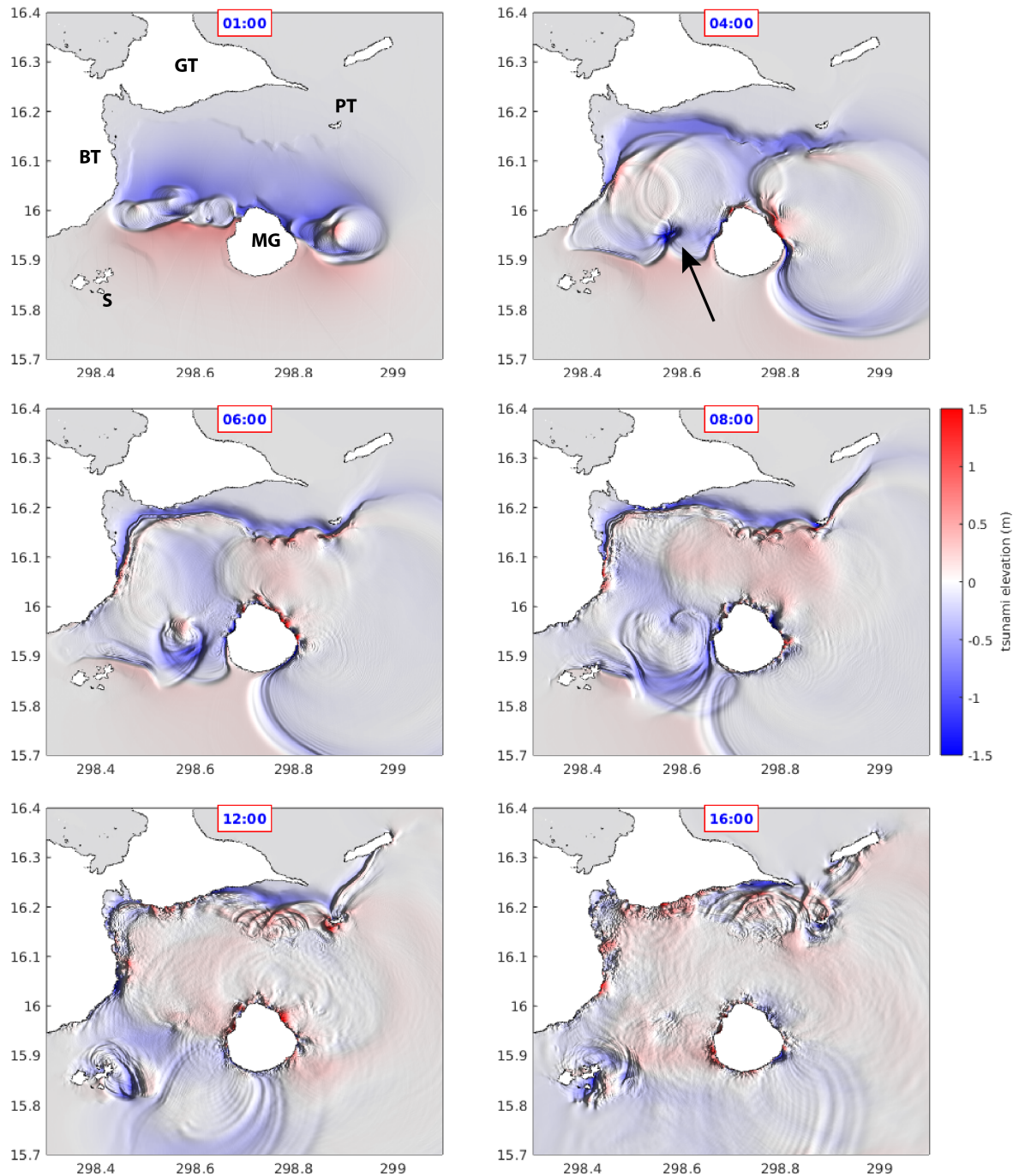


1294 Figure
 1295 6: ROV photographs of fault identified on the seafloor along the BER03-30-31 seismic line across
 1296 the F3' Morne Piton fault segment (location on Figure 3) . (A) photography of the hangingwall of
 1297 F3'. The eroded F3' fault plane presents a progressive downward slope steepening (B and C) until
 1298 the toe of the fault, which is marked by a characteristic co-seismic scarp with a dip slip striae (D E
 1299 F). On each photograph, white numbers starting with a P is the water depth in meters Latitude is
 1300 North and Longitude is West (WGS84). A B and C views show several tens square meters wide areas,

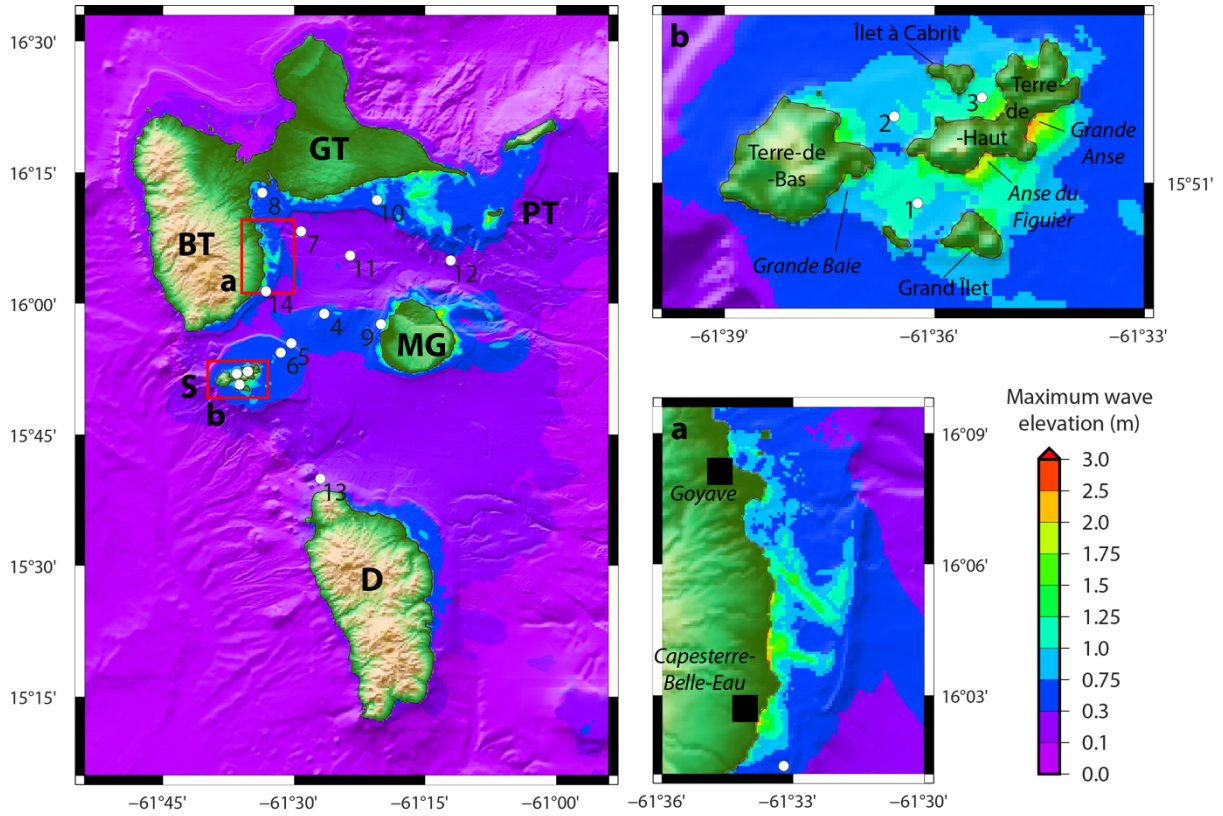
1301 *D E F* are close up showing ca 1m high escarpment just above the foot of the fault scarp (visible at
1302 the bottom of each photos).
1303



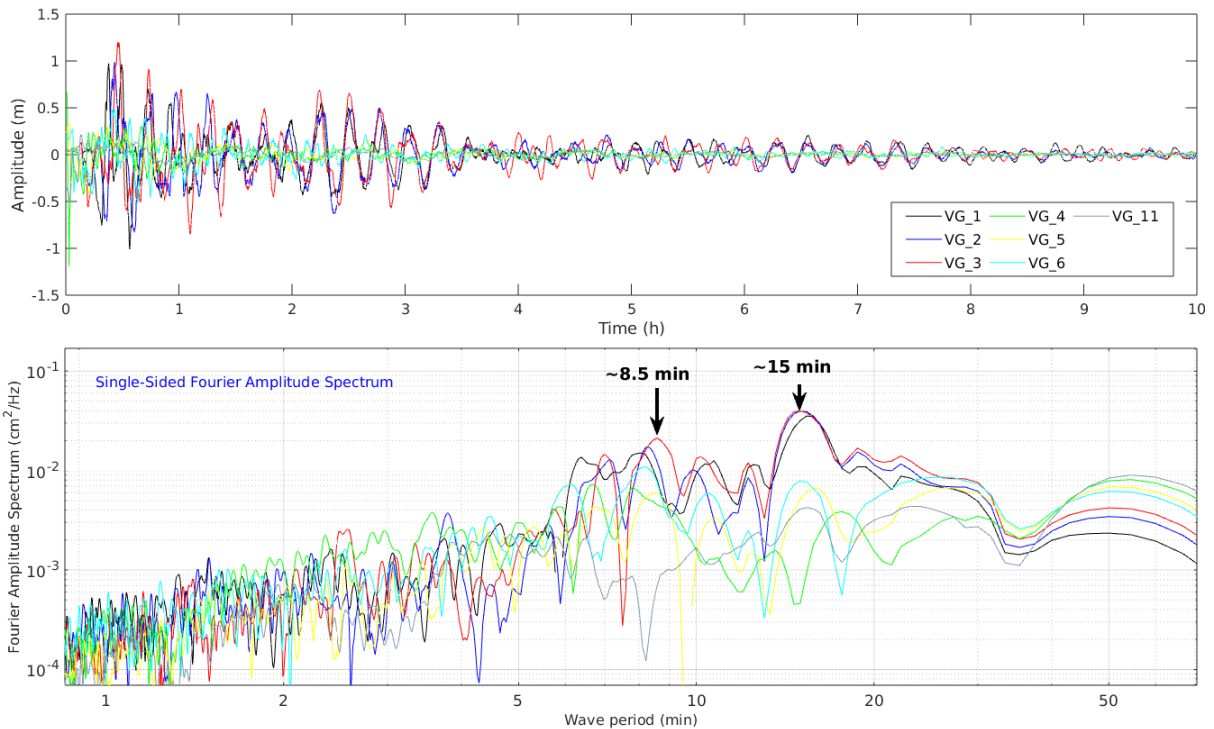
1304 *Figure*
1305 *7: Initial surface elevation for a maximum credible scenario built with the 11 fault segments*
1306 *detailed in Table 3. Blue dots indicate the top fault center. Acronyms stand for Grande-Terre (GT),*
1307 *Basse-Terre (BT), Les Saintes (LS) and Marie-Galante (MG).*



1308
 1309 *Figure 8: Snapshots of tsunami elevation within the Guadeloupe Archipelago at 1, 4, 8, 6, 12 and 16*
 1310 *minutes of waves propagation. Red and blue colors correspond to wave crests and troughs*
 1311 *respectively. The black arrow shows the Banc Colombie shoal. BT: Basse-Terre; GT: Grande-Terre;*
 1312 *S: Les Saintes; PT : Petite-Terre ; MG : Marie-Galante.*

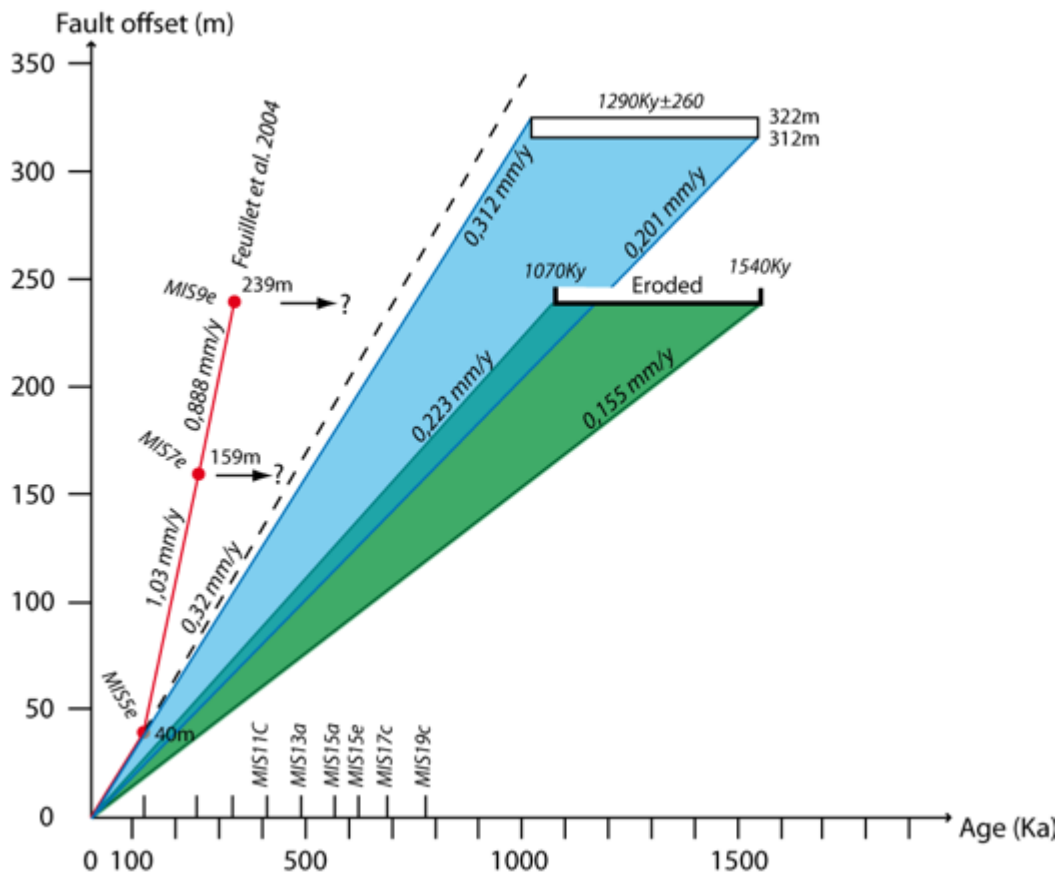


1313
 1314 *Figure 9: Shadowed bathymetric map with tsunami maximum wave elevation. Numbered white*
 1315 *dots: fourteen virtual sea-level gauges (VG) : . BT: Basse-Terre; GT: Grande-Terre; S: Les Saintes; PT*
 1316 *: Petite-Terre ; MG : Marie-Galante ; D : Dominica. VG_4 & VG_11 are located near the fault rupture*
 1317 *region, the VG_5 & VG_6 are near the Les Saintes Fault system. VG_1, VG_2 & VG_3 are within the*
 1318 *Les Saintes archipelago.*



1319

1320 Figure 10: Post-processing of virtual gauge records. Top: sea-level records at 7 different locations
 1321 (VG 1 to 6 and VG11 – location on figure 9); bottom: single-sided Fourier amplitude spectrum. The
 1322 blue arrows symbolize the location of the 2 peaks of period ~6.5 and 17 min.



1323
 1324 Figure 11: Fault offset along the Morne Piton fault against the age of the strain marker. Red: data
 1325 from Feuillet et al. (2004) based on absolute age of terrace T4 (MIS5e), the estimated age of terrace
 1326 T2 (MIS7e) and the suggested age of Marie-Galante upper plateau (MIS9e). Green: strain range
 1327 calculated using upper plateau unit age from Münch et al. (2014) (note that erosion may lower this
 1328 estimation strain rate). Blue: strain range calculated from the fault offset of the seismic unit dated
 1329 ca 1,2Ma along the seismic line K08-59 (green reflector on Figure 4). Dotted line indicates the 0.32
 1330 mm·yr⁻¹ strain rate from the estimated offset of the MIS5e Terrace in Marie-Galante (Feuillet et al.
 1331 2004).
 1332

Cruise	KaShallow 1	KaShallow 2	Aguadomar	SismAntilles	GEOBERYX03 SISM BGM
Seismic source	1000 J sparker	35-45 in3 GI Airguns array	45-105 in3 Two GI Airguns	4400 in3 Airguns array.	1000 J sparker
Peak frequency (far field)	250-400Hz	40-70Hz	30-50Hz	15-20Hz	250-400Hz
Number of traces	6 traces	72 traces	6 traces	360 traces	6 traces
Fold coverage	3/6 fold	9/18 fold	3 fold	30 fold	3/6 fold
Inter CDP distance	4 m	3.125 m	4 m	6,25 m	4 m

1333
1334 *Table 1: Main acquisition parameters of the seismic data shown in this study (Figures 4 and 5).*
1335

Profile Name Ported from East to West	Age	Uncer tainty (Ma)	horizon depth in the footwall (stwt)		horizon depth in the hangingwall (stwt)		Ven m/s 2500		Ven m/s 2500		Ven m/s 2000		Ven m/s 2000		Strain rate (mm/years)			Interval strain rate (mm/yrs)
			water	rock	water	rock	max	min	max	min	min	max	Average	min	max	nty		
																	max	
K09-44-45 – MG-SB2	16	1	1,575	0,83	1,575	1,2	2 212,5	2 700,0	2 006,3	2 396,3	487,5	390,0	0,046	0,089	0,067	0,030		
since inception	7	1,5																
K09_08-09 – MG-SB2	16	1	0,595	0,91	1,27	0,9	1 577,5	2 052,5	1 351,3	1 832,5	475,0	481,3						
since inception	7	1,5											0,057	0,086	0,071	0,021		
Agua 97 – MG-SB2	16	1	0,05	0,72	1,36	0,6	937,5	1 770,0	757,5	1 620,0	832,5	862,5						
since inception	7	1,5											0,101	0,151	0,126	0,035	0,07	
UB4	2,95	0,05	0,23	0,09	0,59	0,4	285,0	905,0	262,5	812,5	620,0	550,0	0,183	0,214	0,199	0,022	0,16	
K08-059	1,29	0,26	0,22	0,02	0,5	0,1	190,0	512,5	185,0	485,0	322,5	300,0	0,194	0,313	0,253	0,085	0,25	
Ber 03-31	1,29	0,26	0,21	0,04	0,53	0,1	207,5	522,5	197,5	497,5	315,0	300,0	0,194	0,306	0,250	0,079		
K08-24	1,29	0,26	0,25	0,04	0,6	0	237,5	487,5	227,5	480,0	250,0	252,5	0,163	0,243	0,203	0,056		
K09-090	1,29	0,26	0,33	0,02	0,49	0,1	272,5	530,0	267,5	497,5	257,5	230,0	0,148	0,250	0,199	0,072		
K09-096	1,29	0,26	0,32	0,12	0,44	0,1	390,0	505,0	360,0	470,0	115,0	110,0	0,071	0,112	0,091	0,029		

1337 *Table 2: Measured offset of seismic reflectors across the Morne Piton fault system and calculated*
1338 *total vertical strain rates. See text for the ages estimate. Seismic reflectors depth on each side of the*
1339 *fault system is measured in time (stwt – second two way time) and converted in depth in using water*
1340 *velocity (1500m/s) and two end-member velocities for the sediment (see text for explanation),*
1341 *providing a minimum and a maximum offset value. The minimum strain rate is obtained from the*
1342 *ratio between the min offset and the max age bound of the reflector and vice versa.*
1343

Fault segment	Lon (°)	Lat (°)	Length (m)	Width (m)	Top of the fault plane depth (m)	Strike (°)	Dip (°)	Rake (°)	Slip (m)
F1	-61.5335	15.98987	2838	12500	500	111	75	-90	1.89
F2	-61.4708	15.994	9070	12500	500	78	75	-90	1.89
F3'	-61.4428	16.01503	3918	12500	500	95	75	-90	1.89
F3	-61.4108	15.99009	3474	12500	500	88	75	-90	1.89
F4	-61.377	15.99367	2735	12500	500	84	75	-90	1.89
F5	-61.3287	15.99021	6623	12500	500	97	75	-90	1.89
F6	-61.2846	15.97275	4813	12500	500	128	75	-90	1.89
F7	-61.2301	15.95767	7904	12500	500	92	75	-90	1.89
F8	-61.1477	15.94221	4052	12500	500	92	75	-90	1.89
F9	-61.1042	15.94958	5495	12500	500	70	75	-90	1.89
F10	-61.111	15.93014	5336	12500	500	78	75	-90	1.89
F11	-61.0777	15.94126	2228	12500	500	52	75	-90	1.89

1344
1345 *Table 3: Parameters used for the tsunami source simulation of a rupture along the multisegment*
1346 *fault presented in figure 7.*
1347